PALEOENVIRONMENTAL CONSTRAINTS ON PLEISTOCENE ICE SHEETS FROM GLACIO-VOLCANIC DEPOSITS IN NORTHEAST ICELAND

by

Cameron D. Essex

A Thesis Submitted in

Partial Fulfillment of the

Requirements for the Degree of

Master of Science

in Geoscience

at

The University of Wisconsin-Milwaukee

August 2024

ABSTRACT

PALEOENVIRONMENTAL CONSTRAINTS ON PLEISTOCENE ICE SHEETS FROM GLACIO-VOLCANIC DEPOSITS IN NORTHEAST ICELAND

by

Cameron D. Essex

The University of Wisconsin-Milwaukee, 2024
Under the Supervision of Professor Barry Cameron

There are indications that the melt-back of glaciers due to climate change can trigger new eruptions for volcanoes and magma reservoirs that rest under ice sheets. The ideal locality on Earth to study volcano-ice interactions is Iceland, an active volcanic island that has been totally covered in previous ice ages. Eruptions under glaciers produce distinctive landforms called tuyas, or table mountains, which can provide an estimate of ice thickness at the time of eruption. One research tool used to investigate ice thickness is volcanic glass, which is formed from rapid cooling of magma, and thus is abundant in the majority of systems where eruptions occur under or within ice or glacial meltwater. In particular, northeast Iceland has been used as a yardstick for ice thickness estimates using tuyas based on the elevation of capping lava flows and glassy eruptive products, and previous research suggests that ice thickness increases to the south towards Iceland's largest, present-day glacier: Vatnajökull. We hypothesize that ice thickness estimates using volatiles in volcanic glass records a similar story of ice thickness for northeast Iceland, with ice thickness increasing to the south for tuyas closer to Vatnajökull glacier. We report some of the first chemical data for volcanic glasses including water, carbon dioxide, major elements, and sulfur concentrations for four tuyas in northeast Iceland: Gæsafjöll, Búrfell, Bláfjall, and Herðubreið. Major elements and sulfur were analyzed, and the composition of glass for all four tuyas is basaltic, suggesting their formation was due to partial melting of the mantle. However, Búrfell contains a component enriched in FeO and depleted in MgO and CaO, which may be due to different mantle sources or interaction with crystal mushes in tiered sill-like magma reservoirs. Furthermore, Búrfell shows the highest sulfur contents compared to the other three tuyas, suggesting it had more pressure exerted by overlying ice during its formation. Lastly, water content was collected using Fourier Transform Infrared Spectroscopy (FTIR). These data show that low water contents dominate for Gæsafjöll, Herðubreið, and Bláfjall suggesting thin ice during eruption, and slightly higher water contents for Búrfell suggesting thicker ice during eruption, which shows ice thickness did not progressively increase to the south towards Vatnajökull glacier and was more complex than previously thought. Hydrogen isotopes (δD) and water contents reveal volcanic glass in northeast Iceland was a result of open system degassing based on Raleigh fractionation curves, and low water contents and δD values for all four tuyas suggest substantial amounts of water have been lost during degassing. Therefore, this implies that the measured δD values are not those of the original, undegassed parental magmas due to open system processes.

To everyone who has supported me thus far

TABLE OF CONTENTS

LIST OF FIGURES

LIST OF TABLES

ACKNOWLEDGEMENTS

I could not have completed this research alone, and I am indebted to everyone who supported me through this experience. First, I'd like to thank my main advisor Barry Cameron who took a chance and included me to work on this amazing project. Also, my committee members Julie Bowles and Charles Paradis for their support through graduate school and comments to make the writing of this research clear and concise. Additionally, I could not have been able to create an updated map of the study area without the help of a GIS specialist at the University of Wisconsin-Milwaukee: Brett Ketter. Furthermore, I couldn't have done this research without the help of graduate and undergraduate students in the UW-Milwaukee geoscience department. I'd like to thank Ph.D. candidate Chase Glenister for teaching me how to prepare samples for FTIR and EPMA analysis, and any other miscellaneous questions Ihad for lab work. Also, I'd like to thank Cole Schmidt and Maddie Woller who were support for undergraduate research fellows (SURF) students at the time, and helped polish samples for FTIR analysis and were some of the few people who helped me complete the research on time.

In addition, I could not have completed the research without the support of our United States collaborators. First, Will Nachlas at the University of Wisconsin-Madison for EPMA guidance, assistance, and mentoring, as well as Brian Jica at the University of Wisconsin-Madison for ^{40}Ar/^{39}Ar dating of subaerial lava flows. Second, John Robbins and Neil Tabor at Southern Methodist University for hydrogen isotope and water content analysis using manometry. Third, Emily Johnson at the Cascades Volcanic Observatory for using her FTIR for water content analyses. Also, this research could not have been completed without our collaborators at Háskóli Íslands (*University of Iceland*). First, Magnús Tumi Guðmundsson for support and endorsing the Diversity and Innovation Grant through the University of Wisconsin-Milwaukee, an American Scandinavian Foundation Fellowship for an extended field season in the summer 2023 which completed the research for this project, and providing some of the original, crucial sources on the geology of northeast Iceland. Also, Elisa Piispa and Jowita Kumek for paleomagnetic drilling for dating the subaerial lava flows of the tuyas; I could not have climbed to the top of Herðubreið for the last bit of paleomagnetic sampling without Dr. Piispa´s determination.

In addition, I could not have completed the research without additional funding sources. I am thankful to the Geological Society of America Graduate Student Research Grant: Lipman Research Award to support graduate students in volcanology and petrology, as well as the University of Wisconsin-Milwaukee L. Joseph Lukowicz and Nelson Cherkauer Lasca scholarshps for an extended field season in the summer of 2023. Also, the Out to Innovate Career Development fellowship to support professional development of trans, intersex, and non-binary graduate students and post-doctoral fellows in STEM, which will provide funding to attend the Goldschimdt and International Geological Congress conferences in 2024 to disseminate the final results of my master’s research. Finally, I’d like to thank the On To the Future Program through the Geological Society of America and AGQ, the LGBTQ+ affinity group of the American Geophysical Union, for providing a sense of belonging for an early career, queer scientist like me, and of course all my mentors, friends, and family who I could not have gotten through graduate school without and encourage me to lean into other parts of myself that aren’t science (you know who you are)!

1. Introduction

In recent years, accelerating climate change and the melt-back of glaciers and ice sheets have underscored the need for hazard prediction and mitigation to predict future impacts of a warming Earth (Pagli and Sigmundsson, 2008). Surface features, such as moraines and drumlins, along with similar deposits on the sea floor, have been used as indicators of ice thickness but are relatively subtle and typically do not survive successive glaciations. The spatial distribution of ice thickness for ancient glaciers can be calculated into a volume estimate using remote sensing of the elevation of glacio-volcanic deposits (Sigurbergsdóttir, 2023). Ice thickness itself determines a glaciers motion, and hence is behind the glacier's response to climate change. Yet another effective approach to understanding ice thickness in the geological past is to identify the extent and nature of glacio-volcanic deposits. A comprehensive study of glacio-volcanic deposits using major element and volatile geochemistry would improve not only ice thickness estimates of past glaciations, but also record the hydrological properties of the glacial ice sheets and magma evolution of the coeval eruptions. The ideal locality on Earth to study volcano-ice interactions is Iceland, an active volcanic island that has been totally covered by ice in previous ice ages, which have led to the formation of extensive glacio-volcanic landforms (Russell et al., 2014; Werner et al., 1996). The 2010 Eyjafjallajökull eruption highlighted the combination of at least two hazards distinct to glacio-volcanism: local massive flooding and associated tephra production capable of disrupting air travel. The eruption started subaerially in March 2010 when effusive lava flows interacted with snow and ice (Edwards et al., 2012), but then in April 2010, new craters opened under the ice sheet causing explosive eruptions. Furthermore, as opposed to the tuyas (glacio-volcanic landforms) in the northeast, Eyjafjallajökull erupted into relatively thin ice (170–200 m) (Magnússon et al., 2012). Glacio-volcanic deposits can hold information concerning these types of environmental conditions at the time of eruption. One of the main eruptive products used to investigate how lava interacts with ice is volcanic glass, which is formed from rapid cooling of magma, and thus is abundant in the vast majority of systems where eruption occurs under or within glacial ice or glacial meltwater. Volcanic glasses have different H_2O, CO_2, and SO_3 concentrations depending on whether they are generated under thick versus thin ice meltwater conditions. Constraining whether thin or thick ice dominated glacio-volcanism is important to ultimately understanding the nature and history of these potentially hazardous eruptions.

1.1 Background

Eruptions under glaciers produce distinctive landforms called tuyas, or table mountains, (Bemmelen and Rutten, 1955) or “stapi” (Kjartansson, 1943) and can provide an estimate of ice thickness at the time of eruption (Dixon et al., 2002; Höskuldsson et al., 2006; Owen et al., 2017). Some of the first suggestions of this relationship were in northeast Iceland, where abundant magmatism along Iceland’s active northern rift zone led to the production of these landforms (Bemmelen and Rutten, 1955). Previous work utilizing field-based methods observing the elevation of capping subaerial lava flows and glass-rich rocks exposed in tuyas indicates that ice thickness increased to the south towards Iceland’s largest ice sheet: Vatnajökull (Walker, 1965). My work concerns four well-known tuyas in northeast Iceland along a N-S transect towards Vatnajökull: Gæsafjöll, Bláfjall, Búrfell, and Herðubreið (Fig. 1). Some of the earliest accounts of this area suggested that these tuyas were instead nunataks rather than eruptions into ice (Bemmelen and Rutten, 1955). The preservation of volcanic glass within the tuyas leads one to believe otherwise, but the lithologies and morphology of these landforms may also be used to assert their glacio-volcanic origin. The gentle inclinations at the top of the tuya above the sharp, steep cliffs suggested a glacially scoured origin or ice-confined eruptions (Bemmelen and Rutten, 1955). In short, tuyas have been used as a yardstick for ice thickness in studies over the past few decades, but the lava flows and glass-rich rocks have not been further investigated by modern geochemical studies of volcanic glass in northeast Iceland.

Some of the first experiments done using volcanic glass and volatiles to infer eruption depth were basaltic glasses erupted on the sea floor along mid-ocean spreading centers or the submarine flanks of Kilauea shield volcano (Dixon et al., 1988; Coombs et al., 2006). Volatiles in volcanic glass show a range of carbon dioxide (CO_2) and water (H_2O) concentrations at different depths based on the pressure-dependence of volatile solubility in magma, which have motivated others to test this hypothesis on ice thickness estimates in complex glacio-volcanic eruptions, such as those in Iceland (Owen et al., 2018). It's important to quantify the thickness at which the eruption started because predictions can be made with future eruptions under ice. If an eruption started at a certain ice thickness, then monitoring other volcanoes that rest under ice with similar ice thickness more closely would be crucial to hazard planning. Based on field observations, early estimates of Bláfjall record an ice thickness of at least 600 m using the top plateau as the minimum thickness the cap lava breached to the surface (Bemmelen and Rutten, 1955).

Using remote sensing to understand the stratigraphic relationships for the elevation of capping lava flows of tuyas has been a modern technique to quantify past ice thickness and give an estimate of ~700 m of ice thickness for one of the tuyas in the study area: Bláfjall (Fig. 1) (Sigurbergsdóttir, 2023). Tuyas show a transition zone from hyaloclastite deposits (water or ice interaction) to subaerial lava cap (ice free), and so these stratigraphic relationships have been used to give a rough estimate where the eruption breached the ice or meltwater to start forming lava flows instead of glacio-volcanic deposits; therefore, the elevation of the subaerial lava flow cap on the tuya is the minimum ice thickness estimate. On the other hand, Kistufell, another famous tuya in northeast Iceland close to the Vatnajökull ice cap, was evaluated using the subaerial-capping-lava technique to estimate ice thickness (Breddam, 2002). It suggests an actual icecap thickness ˜600–700 m (Breddam, 2002), similar to Bláfjall. This might mean that ice thickness would not decrease to the south assuming the edifices erupted at the same time (Walker, 1965). However, FTIR data from Kverkfjöll—another tuya on the northern margin ofo Vatnajökull—shows high water contents in basaltic glasses indicating ice thicknesses of ca. 1,300–1,600 m (Höskuldsson et al., 2006), which is twice as much as Kistufell, yet at a similar latitude as Kverkfjöll. This ice thickness disparity raises the question whether tuya formation is coeval not. Similar age dates may show that Bláfjall and Kistufell formed at similar times, then water content of glasses would further support the hypothesis that ice thickness increases to the south towards Vatnajökull glacier.

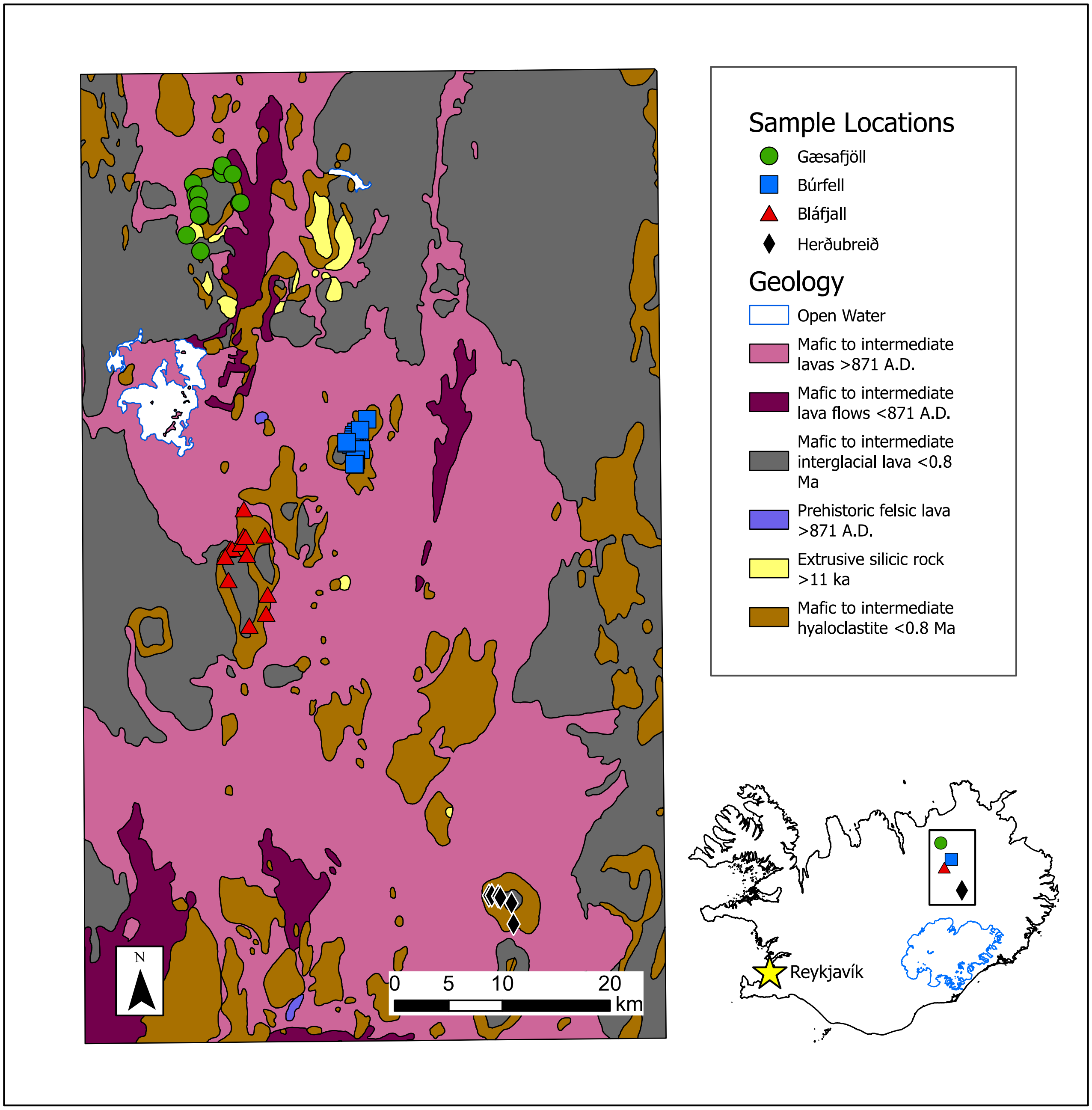

Fig. 1: Geological map of northeast Iceland via ESRI (Environmental Systems Research Institute) and ÍSOR (Iceland GeoSurvey). Sample locations collected for this study are shown with different colored symbols; geological map units are shown by colors as indicated in the legend. Whole Iceland map in lower right shows the study locations in relation to Reykjavík, Iceland's capital, and Vatnajökull (blue outline), Iceland's largest glacier. Northeast Iceland rests along the northern volcanic zone, and also can be divided into fissure swarms: Krafla, Fremrinámar, and Askja (Hjartardóttir et al., 2012). Bláfjall and Gæsafjöll overlap Krafla, Búrfell overlaps Fremrinámar, and Herðubreið overlaps Askja.

1.2 Geologic Setting

Iceland is an active volcanic island that sits at high latitude in the North Atlantic, which has led to the production of frequent volcanic eruptions that have interacted with glacial ice and meltwater. Iceland is young compared to the long history of geologic time, with the oldest rocks just ~25 Ma and the oldest rocks exposed at the surface ~14–16 Ma (Thordarson & Höskuldsson, 2014). However, in northeast Iceland, there has been debate on the age of the rocks in this region. Current maps suggest this area to be less than 0.8 Ma (Fig. 1), but accurate ages are still being debated. For example, cosmogenic ages of sub-aerial exposed lavas at each of the four tuyas were determined in northeast Iceland (Licciardi et al., 2007). This technique relies on the exposure dating of sub-aerial lavas that cap the tuya by measuring cosmogenic nuclides; in this case, ^{3}He is used because it provides significantly less error compared to other nuclides. This method was preferred to reconstruct the geologic history of this area because ^{40}Ar/^{39}Ar of basalt lavas in Iceland are troublesome owing to notoriously low potassium contents, the radiogenic precursor for ^{40}Ar. Cosmogenic ages of the sub-aerial lavas were found to be 14.4±1.0 ka for Gæsafjöll, 10.8±0.3 ka for Búrfell, 10.5±0.6 ka for Herðubreið, and 14.4±0.4 ka for Bláfjall (Licciardi et al., 2007). These ages make initial sense because they occur during a transition period from glacial conditions to interglacial conditions in Iceland. The warming after the Younger Dryas glacial period and the Bølling-Allerød warming period suggest that glacial unloading due to the onset of a warmer climate may have triggered these volcanic eruptions (Licciardi et al., 2007).

Zircon age dates for Gæsafjöll have been collected, and reveal a more complex magmatic history (Hampton et al., 2021). The map presented in Fig. 1 shows that mafic to intermediate lavas and mafic to intermediate hyaloclastite dominate Gæsafjöll tuya.

Additionally, there are rhyolite domes or extrusive silicic rocks at the southwest flank of Gæsafjöll (Fig. 1). These rhyolites have a ^{238}U-^{230}Th-^{232}Th age of 85.5±9.4 ka, and overlapped with an $^{40}Ar/^{39}Ar$ age range of 83–90 ka. No systematic variation between inner and outer cores of the zircon crystals suggests no recycling that would change the ages drastically (Hampton et al., 2021). This is much older than the proposed cosmogenic ages, which may give speculative results owing to snow cover on the sub-aerial lava flows that essentially reset the geological clock for cosmogenic nuclides since the lava outcrops would then be not exposed to the atmosphere anymore. While the younger ages show more correlation with actual glacial and interglacial periods, the zircon dates suggest an otherwise older, warmer era when these eruptions coincided with the onset of a smaller, less extensive ice sheet based on geomorphology of the extent of glacial deposits during this time (Thordarson and Höskuldsson, 2014). The Pleistocene ages shown by the zircons reveal a time period where Iceland is suggested to be covered by ice during the Early Weichselaian glacial maximum (90–80 ka; Svendsen et al., 2004).

However, it is unclear if these zircons crystallized in the magma chamber of the parent magma or just before an eruption. Zircon has been used to help date historic silicic eruptions in Iceland, and some of the crystal ages predate known eruption dates by thousands to tens of thousands of years (Carley et al., 2011). This may beg the question if zircon is a reliable tool to date glacio-volcanic deposits when the lava was emplaced at the surface compared to an older crystallization age in the magma chamber. Zircon ages may not be as useful to calculate when tuyas in northeast Iceland formed, especially whether or not they erupted into ice, which is fundamental for ice thickness estimates.

2. Methods

Three methods were used to analyze the volatile contents in the volcanic glasses: sulfur and chlorine by electron microprobe analysis (EMPA), H_2O and CO_2 manometry, and H_2O by Fourier Transform Infrared (FTIR) Spectroscopy. Fresh glass chips from the glaciovolcanic deposits were hand-picked and stored in 10 mL vials for easy access when mounting for polishing.

2.1 Electron Microprobe

First, for Electron Microprobe Analysis (EMPA), a power drill was used to drill numerous holes 2 mm in diameter and 2 mm deep in a 10 cm aluminum billet to house the glass chips for individual samples. A mount map was made to keep track of which sample resided in which drill hole. The glass chips in the mount were then covered in epoxy and placed overnight in a furnace at 45°C to cure the epoxy. The mount was then polished using standard sets of polishing paper. Analyses was conducted at the University of Wisconsin-Madison's EMPA laboratory using the Cameca SX-Five FE-EMPA with 3–30 kV accelerating voltage and 0.1–700 nA beam current.

Analyses for one of the mounts with just Herðubreið and some Gæsafjöll and Búrfell samples had low totals (e.g., 90% instead of 99% or 100%) during a second analytical session in May 2024 compared to our first probe session in April 2023 with normal totals. There may have been a charging issue when the samples are inserted into the microprobe for analysis. Samples need to be conductive so the electrons can be diverted off the sample immediately and collected in the spectrometers when the X-rays are excited by these electrons; these show the totals for the different major elements of interest. One solution to remedy this is to place pieces of copper tape near the sample so they can be conductive, and X-rays can be collected correctly. The glass may be highly altered when totals are between 90%–97% (Cogliati et al., 2021), and a Chemical Index of Alteration may be used to characterize how altered the samples are. Furthermore, when analyzing the crystals in the glass (e.g., feldspars), the mineral totals were at or above 99%. This suggests that there may not have been charging issue and nothing wrong with the sample mount, since the feldspars show accurate totals, and may be due to the properties of the glass itself.

2.2 Fourier Transform Infrared (FTIR) Spectroscopy

Glass chips were hand-picked out of glass-rich fine-grained hyaloclastites, hyaloclastite breccias, and pillow basalts, and were stored in 10 mL vials. Samples need to be doubly polished for FTIR analysis, so the glass chips were mounted on small glass slides using Densply Caulk orthodontic resin powder and liquid. At least three drops of liquid were used on the powder to sufficiently cover the glass chip and the powder encasing the glass chip. Samples were left to set overnight. The resin-chip was then polished with standard sets of polishing paper (80 µm–0.3 µm). The glass chip needs to have a vitreous luster once fully polished and be clear of any polishing paper residue (this is common for glass chips with a lot of vesicles). Next, for the glass chips to be doubly polished, the polished resin mount is flipped and mounted in crystal bond. The crystal bond is chipped off and melted on a slide using a hot plate. Once the crystal bond is melted, the polished resin mount is squeezed into the liquid crystal bond and evenly coated. The crystal-resin-mount cools off quickly and then is ready for its second polish. The sample needs to be polished down to at least to 100 µm—measured using a micrometer—for the glass to be translucent and avoid any crystals during sample analysis. Once this is complete, the glass wafer is ready to be released by dissolving the crystal bond using a hot plate and inserted into the FTIR at the USGS Cascades Volcanic Observatory.

The sample holder can fit five to six glass chips on a ~5 cm in diameter glass (silica) circle slide so the infrared beam can pass through and record the absorbance of the glass in the detector. The absorbance peaks we are interested in this study are the 3,540 cm^{-1}, 2,350 cm^{-1}, and 1,630 cm^{-1} peak. 3,540 cm^{-1} is for total water content, 2,350 cm^{-1} is for carbon dioxide content, and 1,630 cm^{-1} is for molecular water content (Fig. 2). Moreover, interference fringes in reflectance mode allows the thickness of the glass wafer to be determined accurately (Nichols and Wysoczanski, 2007). The data that is then recorded by the FTIR with particular focus on the water and carbon dioxide wavelengths and the attendant absorbance peak heights; these data are used to calculate water and possibly carbon dioxide content.

Peak heights were converted into water contents using the Beer-Lambert Law:

$$C_i = \frac{M_i Abs}{d\rho\varepsilon} \qquad \text{Equation 1}$$

where *i* refers to the volatile species of interest, M_i is molecular weight, *Abs* is absorbance (measured peak height), *d* is the sample thickness (in µm using a micrometer), ρ is sample density for basaltic glass based on the major element composition (in kg m^{-3}) and ε is the absorption coefficient (1 mol^{-1} cm^{-1}).

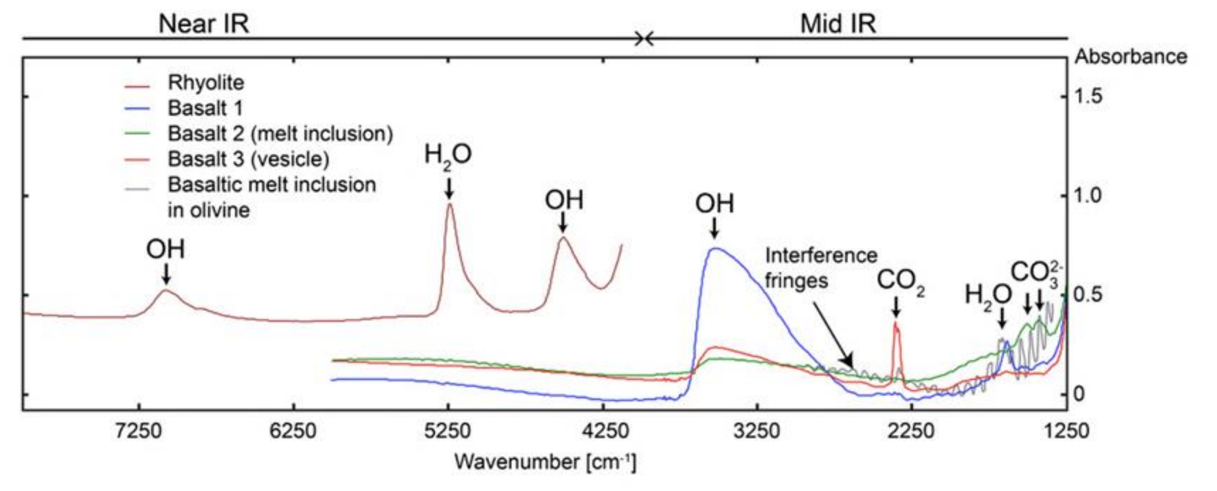

Fig. 2: Spectra of volcanic glass in the near- and mid-infrared regions (Von Aulock et al., 2014). This study focused on basaltic glass, so a typical spectrum we would see using FTIR is the blue line.

2.3 Manometry

Manometry, or bulk extraction, involves heating up earth materials (e.g., volcanic glass) to high temperatures in a short amount of time to capture the volatiles such as carbon, water, and hydrogen released from the heated glass. The glass samples need to be crushed in order to analyze, and I used a lead mortar and pestle to grind the sample to fine-grained particles. I saved two 10 mL vials when grinding: one for the hydrogen manometry analysis, and one for carbon. For hydrogen manometry, the recommended grain size is >200 µm and for the carbon manometry it is <200 µm. After each sample was crushed and sieved properly, the sieve, mortar and pestle, beakers, and petri dishes used to transfer and pulverize the sample were washed with acetone.

Once the sample is secure in a vial and chemically treated with hydrogen peroxide to remove organics, it is ready for extraction. For the hydrogen line, we needed to make a crucible out of a sheet of molybdenum in order for the sample to be held in the extraction line. Additionally, I made a mini-border-tube, 1-inch by 1.5-inch, to secure the crucible and the sample so it doesn't leak out of the pore space created by the strands. The border needs to fit into the crucible and stay secure—this is tested by holding the crucible upside-down, and if it falls out, it needs to be tighter in the crucible. Once these steps are completed, the sample is ready to go into the hydrogen line at the Stable Isotope Laboratory at Southern Methodist University.

The hydrogen line needs to be prepared so all gases from the previous sample are evacuated and ready for a new sample. Once that is done, the sample is inserted to the line in a larger glass tube coated with vacuum grease so no gas can escape. An Ultra Flex vibrator is then turned on to rapidly heat the molybdenum to >1,000°C in mere seconds to fuse the glass chips.

3. Results

3.1 Major Elements and Volatiles with Electron Microprobe

Results of EMPA show trends in both major elements and sulfur (SO_3) concentration. Major element and SO_3 concentrations are reported in Appendix B. Data from EMPA were collected for all four tuyas. Major elements in glassy samples are consistent with tholeiitic basalts (Fig. 3a) for all four tuyas, and while they are all basaltic in their composition, there are distinct and subtle differences in their major element concentrations. The major elements such as FeO, MgO, CaO, Al_2O_3, Na_2O, and K_2O can all be used to show how the most abundant elements in the magma formation are represented for northeast Iceland using linear regression lines (R-squared values in Table 1).

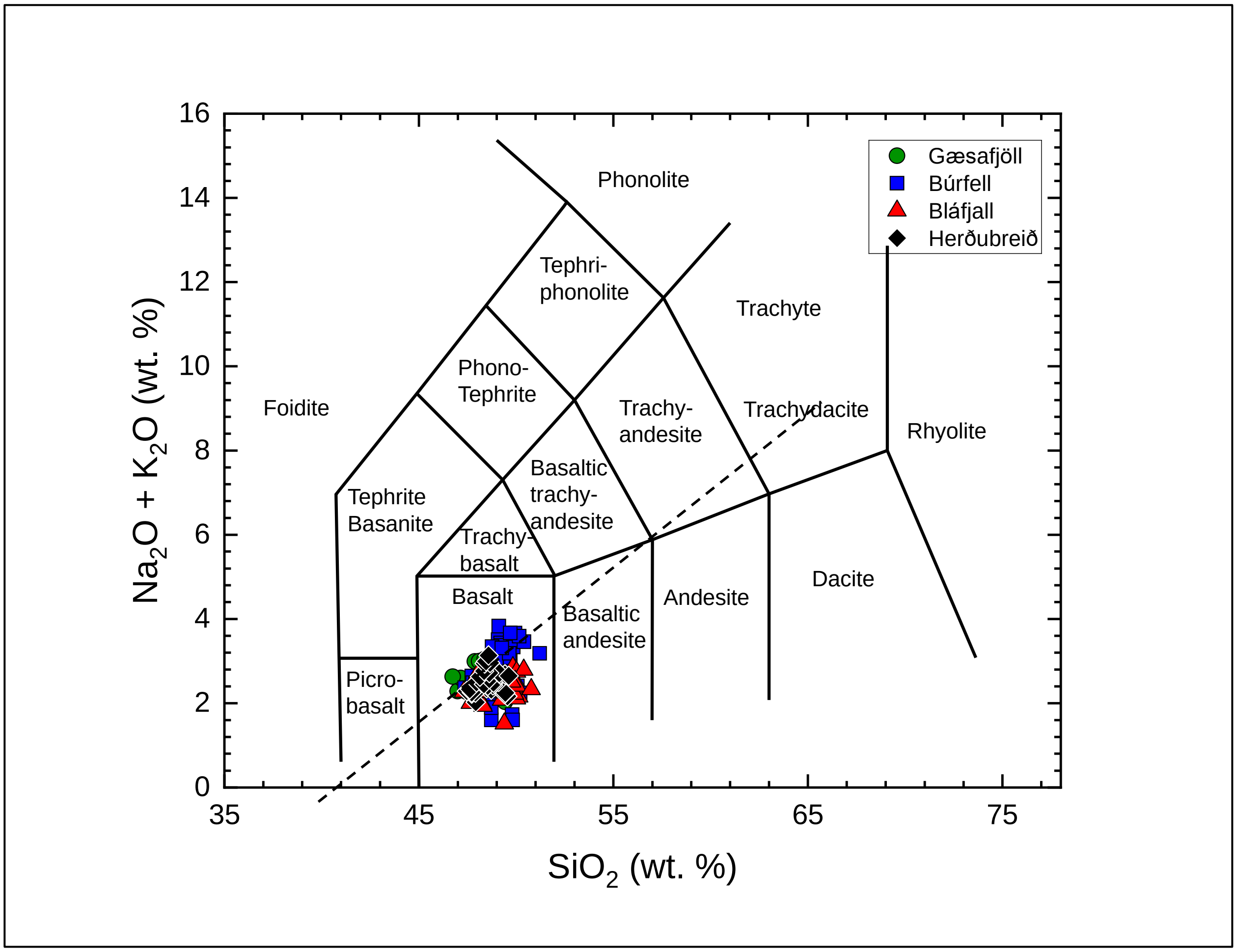

Fig. 3a: Major element chemical classification based on Na_2O+K_2O against SiO_2 (Le Bas et al., 1986). Dashed line shows tholeiitic vs. alkalic basalt (Macdonald and Katsura, 1964); any data below the dashed line is tholeiitic and any data above is alkalic.

Table 1. R-squared values for major elements of linear regression lines

	FeO	**MgO**	**CaO**	**Na_2O**	**K_2O**	**Al_2O_3**	**TiO_2**
Gæsafjöll	0.217	0.254	0.526	0.059	0.236	0.038	0.006
Búrfell	0.574	0.133	0.135	0.006	0.138	0.104	0.098
Bláfjall	0.368	0.037	0.473	0.057	0.001	0.022	0.02
Herðubreið	0.01	0.008	0.003	0.001	0.001	0.038	0.075

3.1.1 FeO vs. SiO_2

For FeO, each of the tuyas show some overlap with respect to how FeO varies in the magma (Fig. 3b). Gæsafjöll has SiO_2 contents ranging from 46.74–50.54 wt. % and FeO from 11.14–13.35 wt. %; Búrfell has SiO_2 contents 47.35–51.22 wt. % and FeO 9.05–16.48 wt. %; Bláfjall has

SiO_2 contents 47.30–50.77 wt. % and FeO 9.77–15.05 wt. %; Herðubreið has SiO_2 contents 47.46–49.61 wt. % and FeO 10.38–13.10 wt. % (SiO_2 concentrations are the same for all the other major element plots moving forward). Gæsafjöll and Herðubreið have some of the lower SiO_2 contents compared to Bláfjall and Búrfell, with Búrfell consisiting of the highest SiO_2 contents.

Búrfell samples show some increasing in FeO with increasing SiO_2 content, and this is also similar to Bláfjall; however, Bláfjall has a slight plateau in FeO content around ca. 49 wt. % SiO_2, then appears to increase in FeO slightly but also decrease around 49.5 wt. % SiO_2. Búrfell also has a separate component of high-FeO glasses ca. 14–16 wt. %., and two Bláfjall samples reach the lower end of the high-FeO Búrfell samples. Moreover, there appears to be no increase in FeO content with SiO_2 content for Gæsafjöll, and Herðubreið appears to be slightly decreasing in FeO with SiO_2.

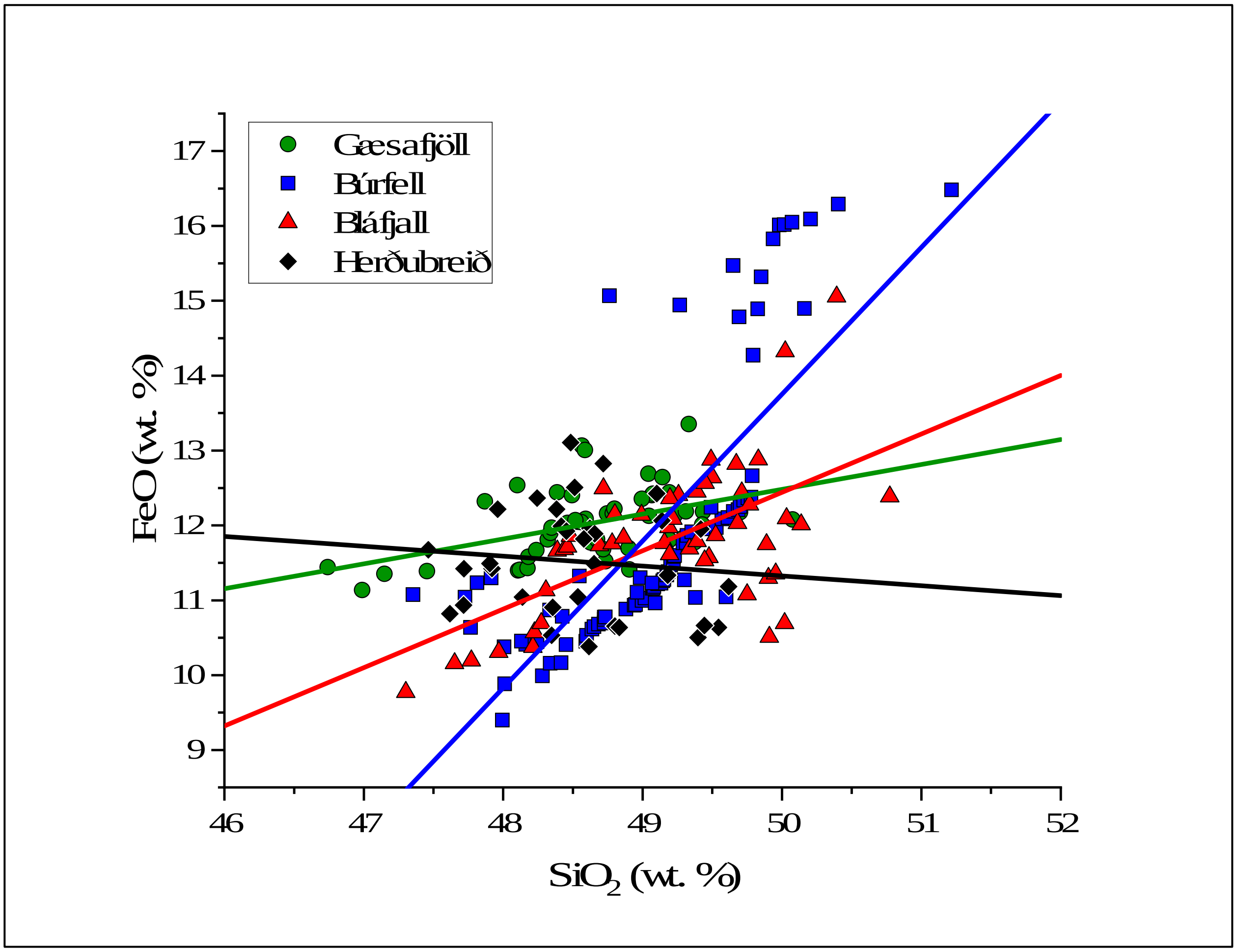

Fig. 3b: FeO vs. SiO_2 for all four tuyas. FeO vs. SiO_2 shows how iron-rich components in the magma have evolved with respect to its silica content. Colored lines show the linear regression for all four tuyas.

3.1.2 MgO vs. SiO_2

For MgO, each of the tuyas show some overlap with respect to how Mg-rich components of the magma evolved underneath northeast Iceland (Fig. 3c). Gæsafjöll has MgO contents 5.98–7.68 wt. %; Búrfell has MgO contents 4.11–9.01 wt. %; Bláfjall has MgO contents 6.81–9.05 wt. %; Herðubreið has MgO contents 5.64–7.66 wt. %. Gæsafjöll and Herðubreið have some of the lowest MgO contents while Búrfell and Bláfjall have higher MgO contents (with some exceptions such as outliers for Búrfell; the lowest MgO point and the two high MgO points). The overall increase in MgO with increasing SiO_2 suggests that olivine is not involved in any crystal fractionation process.

Gæsafjöll shows similar trends with the FeO vs. SiO_2 plot with most points concentrating between 48–49.5 wt. % SiO_2; however, compared to the FeO vs. SiO_2 plot where there were four to five sample points clustered at a higher FeO content in line with Herðubreið, there is the same relationship happening for MgO, but with a lower MgO content. This is also reflected with the two different groups of Búrfell as well. There is a MgO cluster that is consistent throughout near the 8 wt. % MgO content, and there is a lower, 4 wt. % MgO cluster for Búrfell as well; the lower MgO cluster also does not have as many sample points as the high MgO cluster. Herðubreið shows multiple groups of different MgO and SiO_2 contents. For example, there are five to six sample points at 7.5 wt. % MgO, 47.5–48 wt. % SiO_2, four sample points at ca. 5.75 wt. % MgO, ca. 48.25–48.75 wt. % SiO_2, five to six sample points at 7.25–7.75 wt. % MgO, 49.25–49.75 wt. % SiO_2. It seems one of the trends starts to decrease in MgO content with increasing SiO_2 content, with a separate trend that has increasing SiO_2 content but constant MgO content.

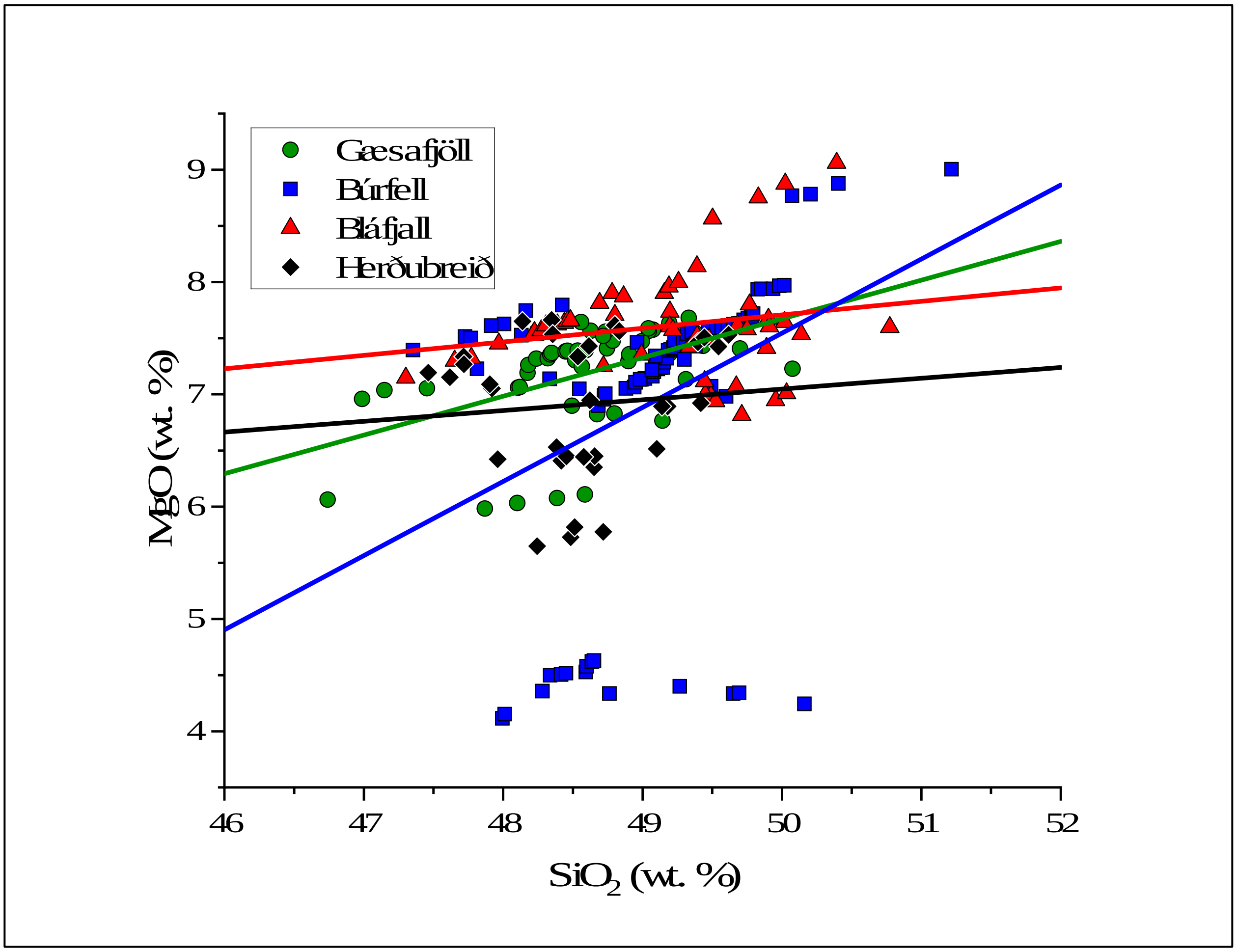

Fig. 3c: MgO vs. SiO_2 for all four tuyas. MgO vs. SiO_2 shows how magnesium-rich components in the magma have evolved with respect to its silica content. Colored lines show a linear regression for all four tuyas.

3.1.3 CaO vs. SiO_2

Again, each of the tuyas show some overlap with respect to how Ca-rich components of the magma evolved underneath northeast Iceland (Fig. 3d). Gæsafjöll has CaO contents 10.80–12.75 wt. %; Búrfell has CaO contents 8.89–13.88 wt. %; Bláfjall has CaO contents 11.19–13.34 wt. %; Herðubreið has CaO contents 10.81–13.05 wt. %.

Overall, Búrfell has the largest range of CaO contents, followed by Gæsafjöll, then Herðubreið and Bláfjall. Gæsafjöll tends to overlap more with Bláfjall as the SiO_2 content starts to increase, compared to Búrfell and Herðubreið. Furthermore, Búrfell also shows two distinct trends again, and there is a high-CaO trend and a low-CaO trend. The low-CaO trend likely corresponding to the high Fe basalts has two separate components: one with SiO_2 content 48–48.75 wt. % and one with SiO_2 content 49.25–50.25 wt. %. The lower SiO_2 content trend shows a slight increase in CaO content reaching its highest SiO_2 endmember; the higher SiO_2 trend is more scattered and shows some sample points with high CaO and low CaO content than the low-SiO_2 trend. Búrfell has the most variation in CaO and SiO_2 compared to the other tuyas. For instance, Herðubreið does have two separtate components of a high CaO trend and a lower CaO trend, but it is not as distinct as Búrfell, and the overall trend for Herðubreið CaO content as SiO_2 content increases is a slight decrease in CaO with SiO_2 (negative correlation). Moreover, while Bláfjall shows an overall trend of increasing CaO with SiO_2, there is also no distinct separation between clusters; however, there could be a subtle difference in the low SiO_2 and low CaO content (47.25–49 wt. SiO_2; 11.5–12.25 wt. CaO) and high SiO_2 and high CaO (49.25–50.50 wt. SiO_2; 12–12.5 wt. % CaO) for Bláfjall.

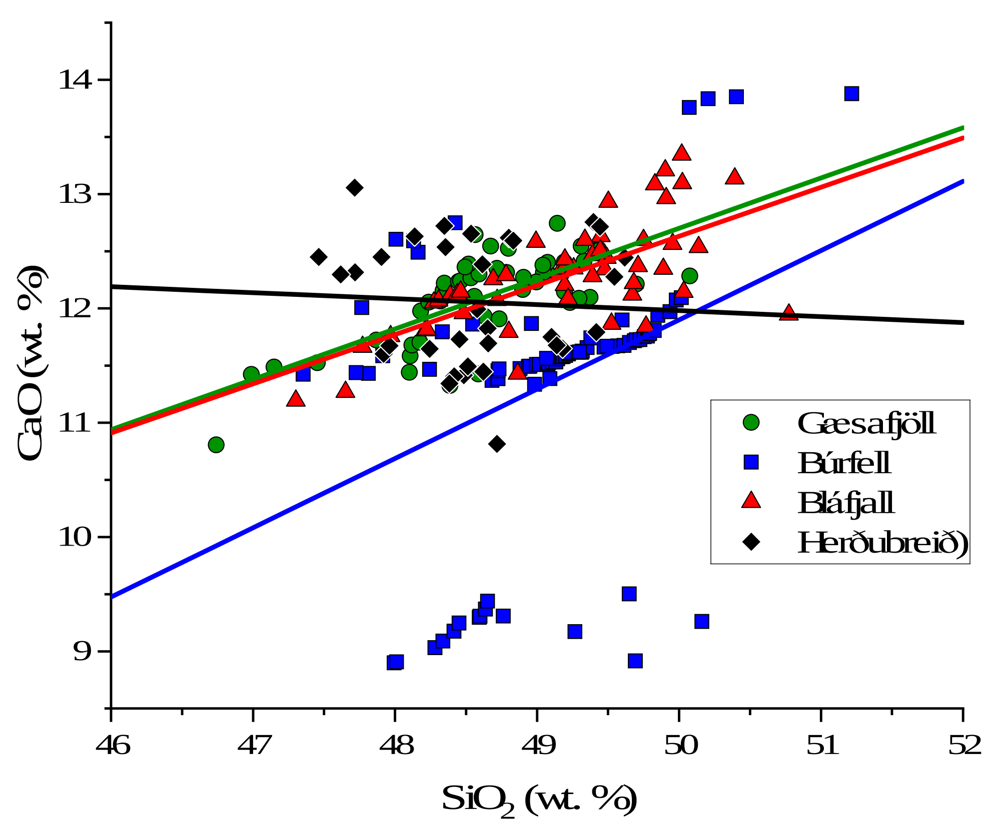

Fig. 3d: CaO vs. SiO_2 for all four tuyas. CaO vs. SiO_2 shows how calcium-rich components in the magma have evolved with respect to its silica content. Colored lines show a linear regression for all four tuyas.

3.1.4 Al_2O_3 vs. SiO_2

Each of the tuyas show some overlap with respect to how Al-rich components of the magma evolved underneath northeast Iceland (Fig. 3e). Gæsafjöll has Al_2O_3 contents 12.73 wt. %–15.04 wt. %; Búrfell has Al_2O_3 contents 12.01–15.77 wt. %; Bláfjall has Al_2O_3 contents 13.35–15.71 wt. %; Herðubreið has Al_2O_3 contents 12.42–14.54 wt. %.

Compared to CaO, FeO, and MgO, Al_2O_3 contents for all four tuyas seem to be relatively consistent with each other. The range of Al_2O_3 content does not deviate as much with varying SiO_2 content; however, Búrfell still does a have two slight separate clusters. For example, there is a cluster that stays consistent with ca. 15 wt. % Al_2O_3 and from 47.5–50.5 wt. % SiO_2, and another cluster with less frequent points that stays consistent ca. 14.5 wt. % Al_2O_3 and from 48.75–50.5 wt. % with one outlier at the same Al_2O_3 content at ca. 51.25 wt. % SiO_2.

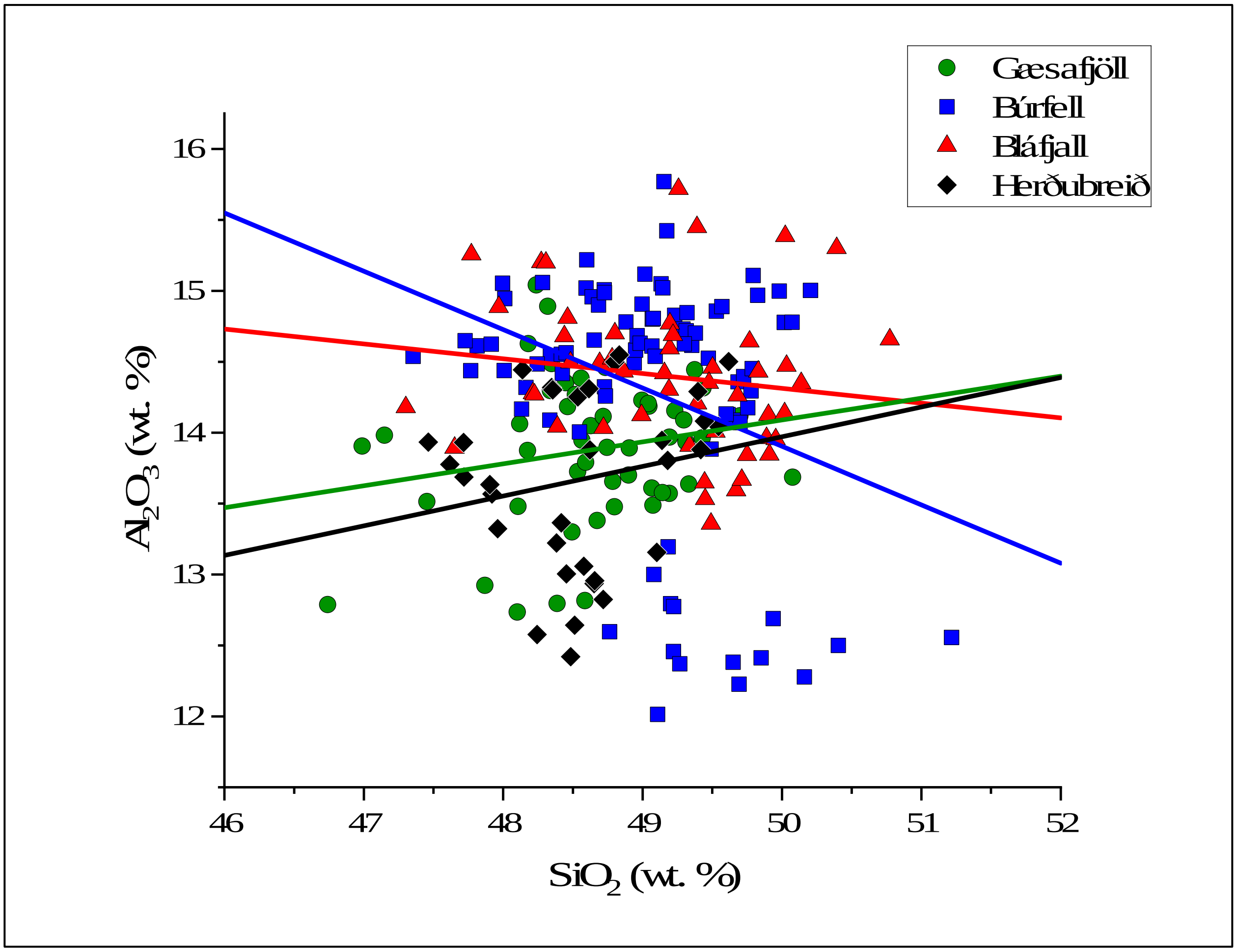

Fig. 3e: Al_2O_3 vs. SiO_2 for all four tuyas. Al_2O_3 vs. SiO_2 shows how aluminum-rich components in the magma have evolved with respect to its silica content. Colored lines show a linear regression for all four tuyas.

3.1.5 Na_2O vs. SiO_2

Each of the tuyas show some overlap with respect to how Na-rich components of the magma evolved underneath northeast Iceland (Fig. 3f). Gæsafjöll has Na_2O contents 1.82–2.64 wt. %; Búrfell has Na_2O contents 1.52–3.54 wt. %; Bláfjall has Na_2O contents 1.48–2.63 wt. %; Herðubreið has Na_2O contents 1.81–2.75 wt. %.

Búrfell has the widest range of Na_2O contents, while Gæsafjöll, Bláfjall, and Herðubreið have similar Na_2O contents with slight differences. Na_2O contents start to increase for some components of Búrfell in the 2.5–3.0 wt. % range as SiO_2 content increases, but Bláfjall's Na_2O content seems to remain constant throughout the whole range of SiO_2 content, with a few outliers that are lower and higher in Na_2O content at varying SiO_2 contents. Furthermore, a separate trend for Gæsafjöll seems to decrease in Na_2O content as overlapping steps as SiO_2 content increases. Herðubreið almost resembles a bell curve of increasing Na_2O as it reaches the midpoint for the range of SiO_2, and then starts to decrease in Na_2O afterwards; however, not all samples follow this increase in Na_2O, and some clusters have slightly decreasing Na_2O content with increasing SiO_2.

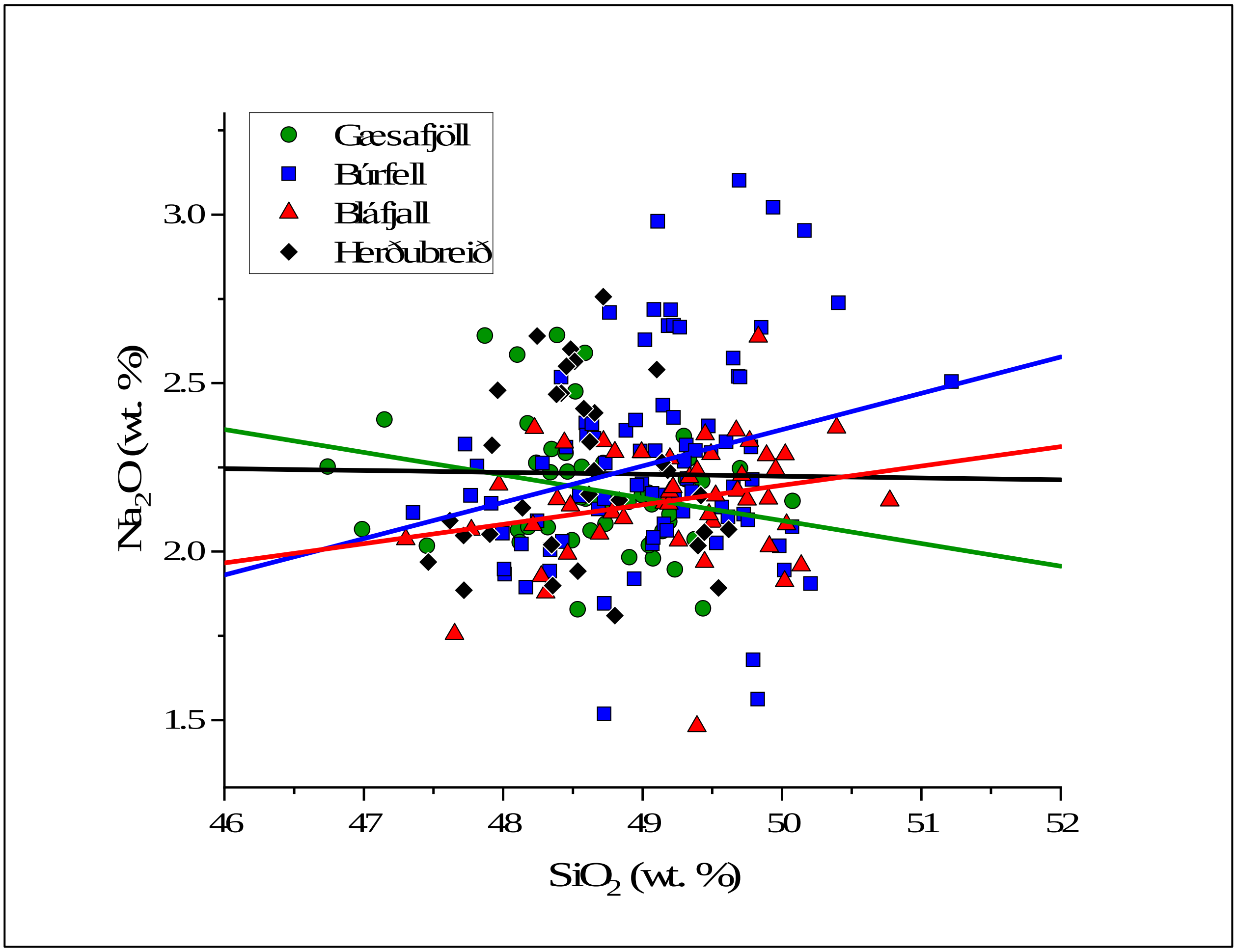

Fig. 3f: Na_2O vs. SiO_2 for all four tuyas. Na_2O vs. SiO_2 shows how sodium-rich components in the magma have evolved with respect to its silica content. Colored lines show a linear regression for all four tuyas.

3.1.6 K_2O vs. SiO_2

Each of the tuyas show some overlap with respect to how K_2O varies in the glasses as the magma evolves (Fig. 3g). K_2O remains uniformly low in tholeiitic basaltic glasses. Gæsafjöll has K_2O contents 0.16–0.418 wt. %; Búrfell has K_2O contents 0.04–0.849 wt. %; Bláfjall has K_2O contents 0.0360–0.466 wt. %; Herðubreið has K_2O contents 0.163–0.520 wt. %.

Overall, Búrfell has the widest range of K_2O content, while Gæsafjöll, Bláfjall, and Herðubreið stick to a general trend; however, there is some slight clusters that show deviation from the trend (constant ca. 0.20 wt. % K_2O over 47–50 wt. % SiO_2). Búrfell tends to make its own trend with most of the data points concentrating between 0.25–0.35 wt. % K_2O and 48–50 wt. % SiO_2. In addition, Búrfell also has a separate component of high-K_2O contents, about twice as high as its general 0.25–0.35 wt. % K_2O trend. In addition, Bláfjall does not have the bimodal characteristic shown by Búrfell, but more of U-shape trend in the data. For example, Bláfjall data points start off with moderately high (0.4 wt. %) K_2O contents with low SiO_2, and then there is a constant K_2O content with increasing SiO_2 until 50 wt. SiO_2 where Bláfjall starts to increase again. For Herðubreið, the K_2O data almost looks like a pyramid shape, with the foundation and most of the data at 0.20 wt. % K_2O and between 47.5–50 wt. % SiO_2, and followed by the second tier cluster of 0.375–0.50 wt. % K_2O between 48–49.25 wt. % SiO_2 that is stacked on top of the lower K_2O cluster.

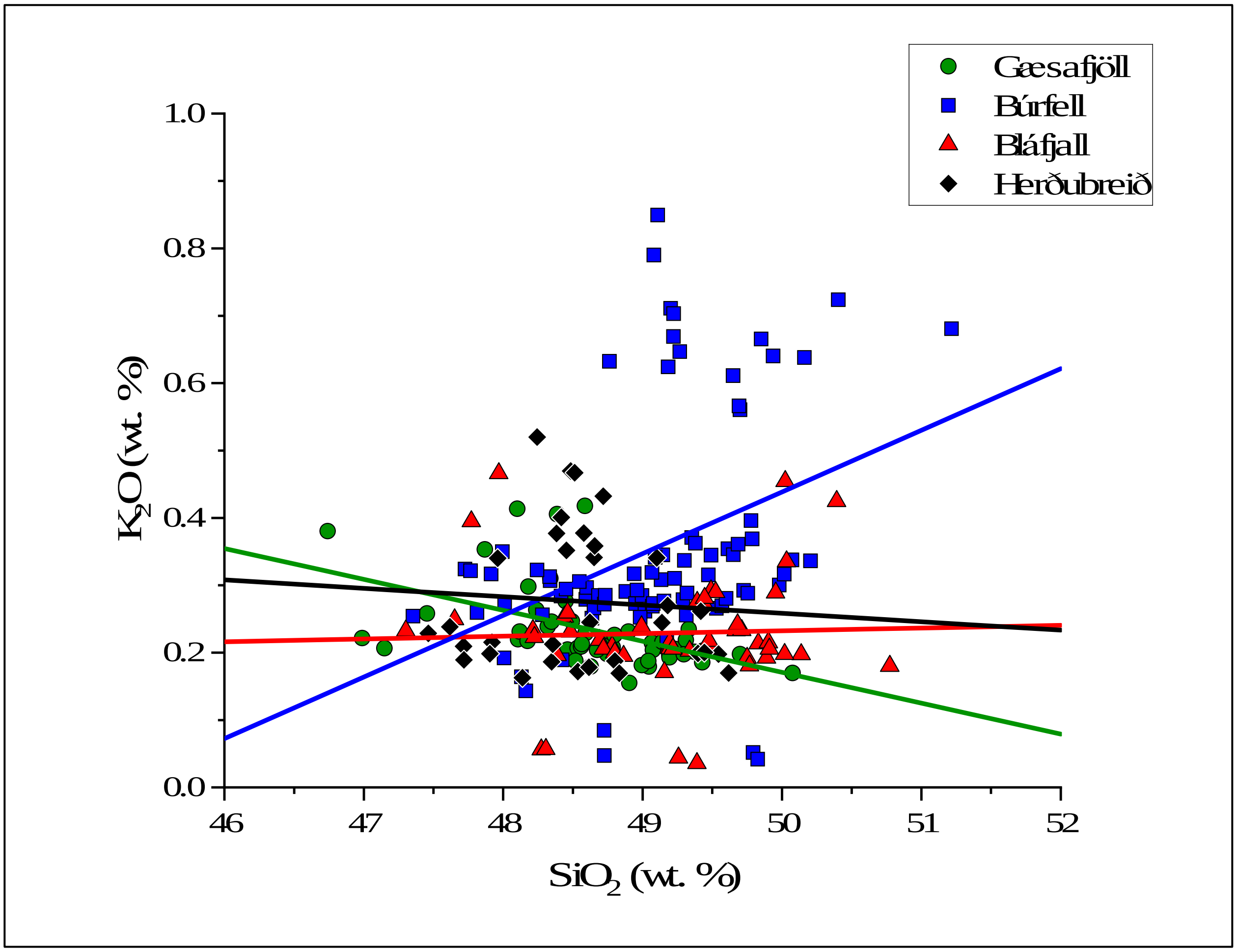

Fig. 3g: K_2O vs. SiO_2 for all four tuyas. K_2O vs. SiO_2 shows how potassium-rich components in the magma have evolved with respect to its silica content. Colored lines show a linear regression for all four tuyas.

3.1.7 TiO_2 vs. SiO_2

Each of the tuyas show some overlap with respect to how TiO_2 varies in the glasses as the magma evolves (Fig. 3h). Gæsafjöll has TiO_2 contents 1.54–2.93 wt.%; Búrfell has TiO_2 contents 0.775–3.19 wt.%; Bláfjall has TiO_2 contents 0.758–2.619 wt.%; Herðubreið has TiO_2 contents 1.44–3.14 wt.%.

Overall, there are scattered relationships for Ti-content for all four tuyas. First, Búrfell has two different clusters of Ti-content: a low-Ti cluster and high-Ti cluster. This is also true for Herðubreið, but the high-Ti cluster for Herðubreið is not as high as Búrfell; the lower Ti-content for Herðubreið also overlaps Búrfell. Gæsafjöll and Bláfjall do not show this split distribution, and have relatively medium Ti-contents, with Gæsafjöll having slightly higher Ti-content compared to Bláfjall. However, Bláfjall still has higher Ti-content for the low-Ti clusters of Herðubreið and Búrfell. For the linear regressions, Bláfjall and Búrfell show a positive correlation with TiO_2 vs. SiO_2 and Herðubreið show a negative correlation, and Búrfell shows a steeper positive slope than Bláfjall while Herðubreið shows a steeper negative slope than Gæsafjöll.

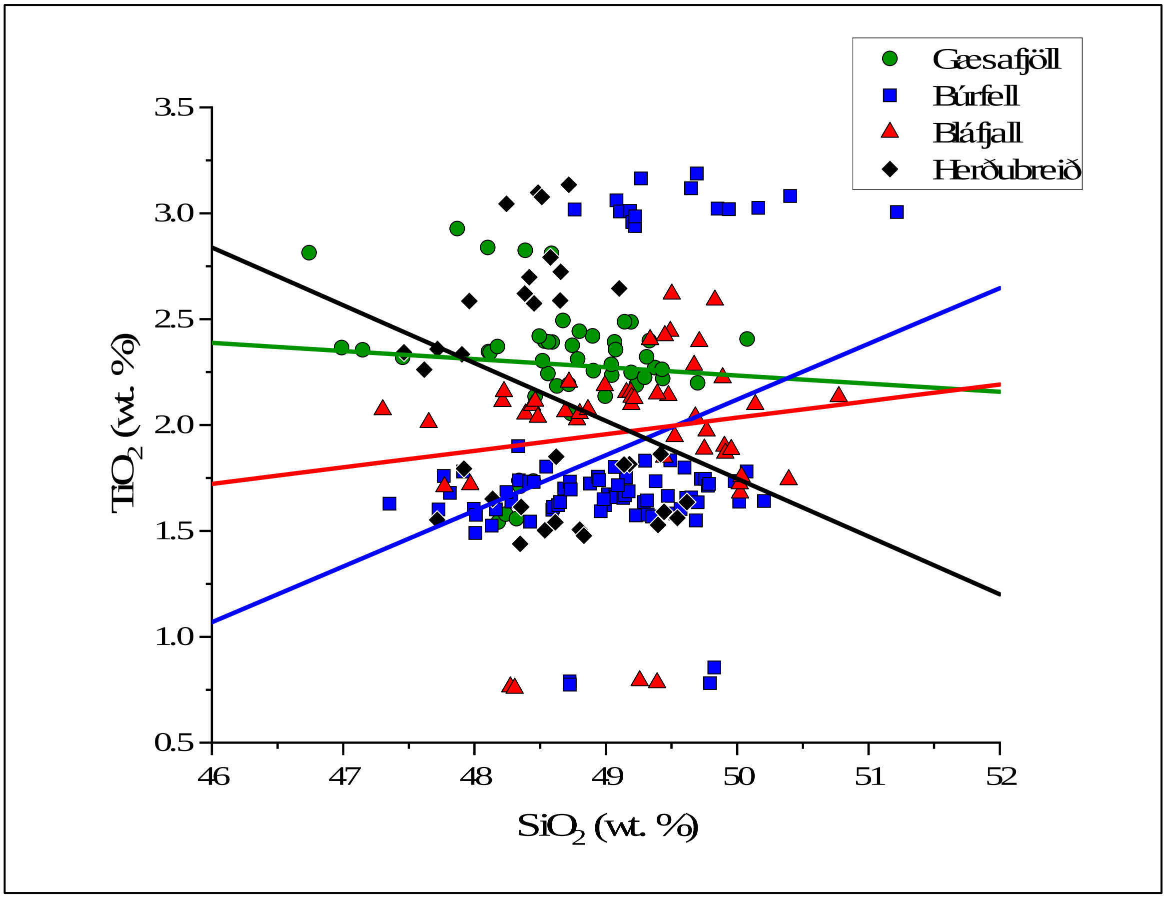

Fig. 3h: TiO_2 vs. SiO_2 for all four tuyas. TiO_2 vs. SiO_2 shows how titanium-rich components in the magma have evolved with respect to its silica content. Colored lines show a linear regression for all four tuyas.

3.1.8 Total SO_3 Content

Each of the tuyas show some overlap with respect to how sulfur components of the volcanic glass preserve a chemical snapshot of the erupted magma (Fig. 4). Gæsafjöll has SO_3 contents 0–1,865 ppm with a mean of 525.7 ppm; Búrfell has SO_3 contents 0–3,002 ppm with a mean of 1.289.1 ppm; Bláfjall has SO_3 contents 0 ppm–2,356 ppm with a mean of 655.1 ppm; Herðubreið has SO_3 contents 0–2,281 ppm with a mean of 585.7 ppm.

Overall, Búrfell shows the highest sulfur contents followed by Bláfjall, Herðubreið, and Gæsafjöll, respectively. Búrfell and Herðubreið show a different distribution compared to Bláfjall and Gæsafjöll. Búrfell and Herðubreið show a consistent increase in sulfur content with respect to it‘s concentration of data points, and do not have gaps like Bláfjall and Gæsafjöll. However, Búrfell does start to show some clustering around 1,500–1,750 ppm, while Herðubreið does not show grouping for these sulfur contents. Furthermore, Búrfell also has consistently higher sulfur contents compared to Herðubreið, despite Herðubreið being the closest to Vatnajökull ice cap. Bláfjall has slightly higher mean sulfur content compared to Herðubreið, even though it is the third closest tuya out of the four to Vatnajökull glacier; Gæsafjöll has the lowest mean and range of sulfur contents out of all the four tuyas and is the furthest from the Vatnajökulll ice cap.

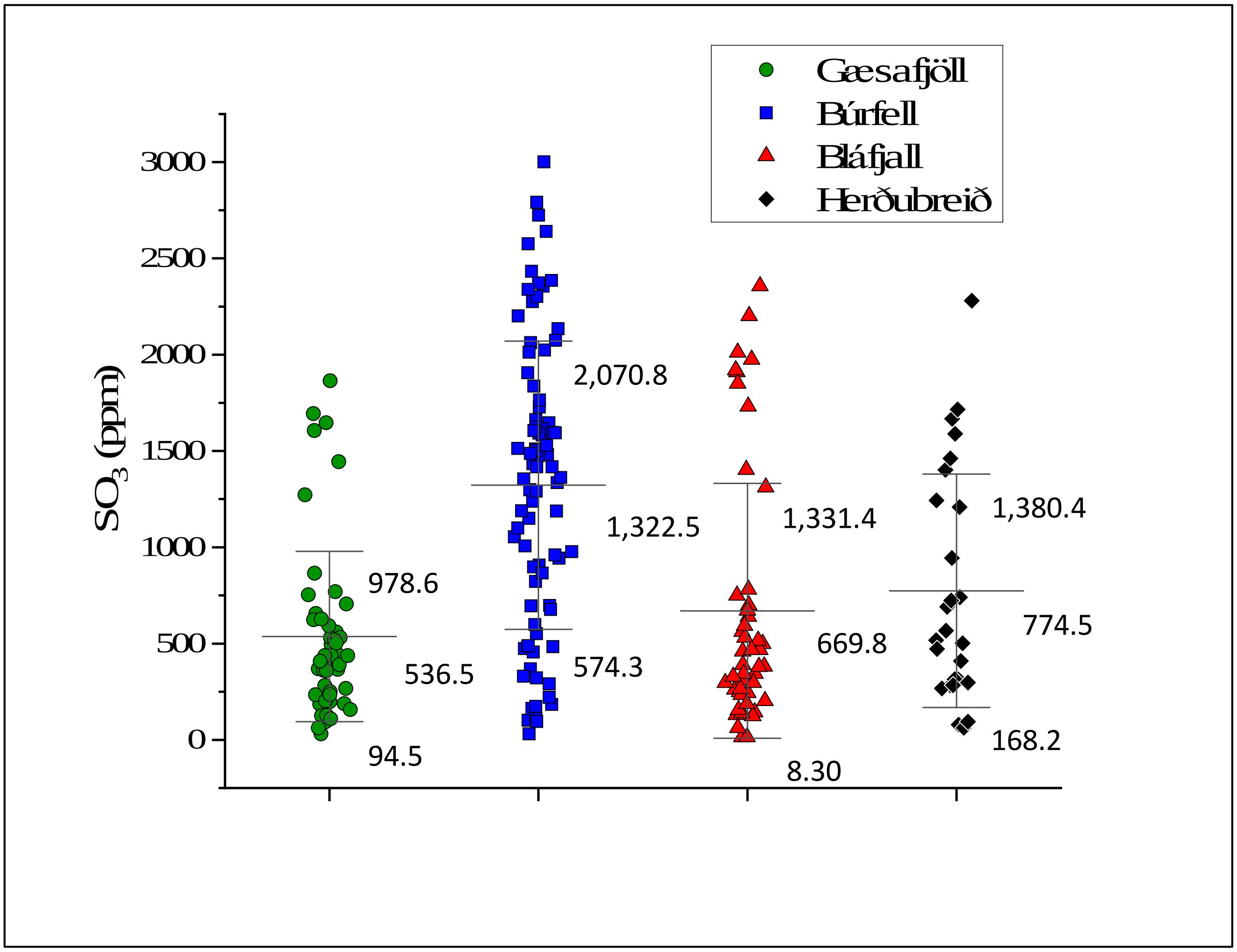

Fig. 4: SO_3 of northeast Iceland volcanic glass. Vertical bars indicate analysis ± 1 standard deviation.

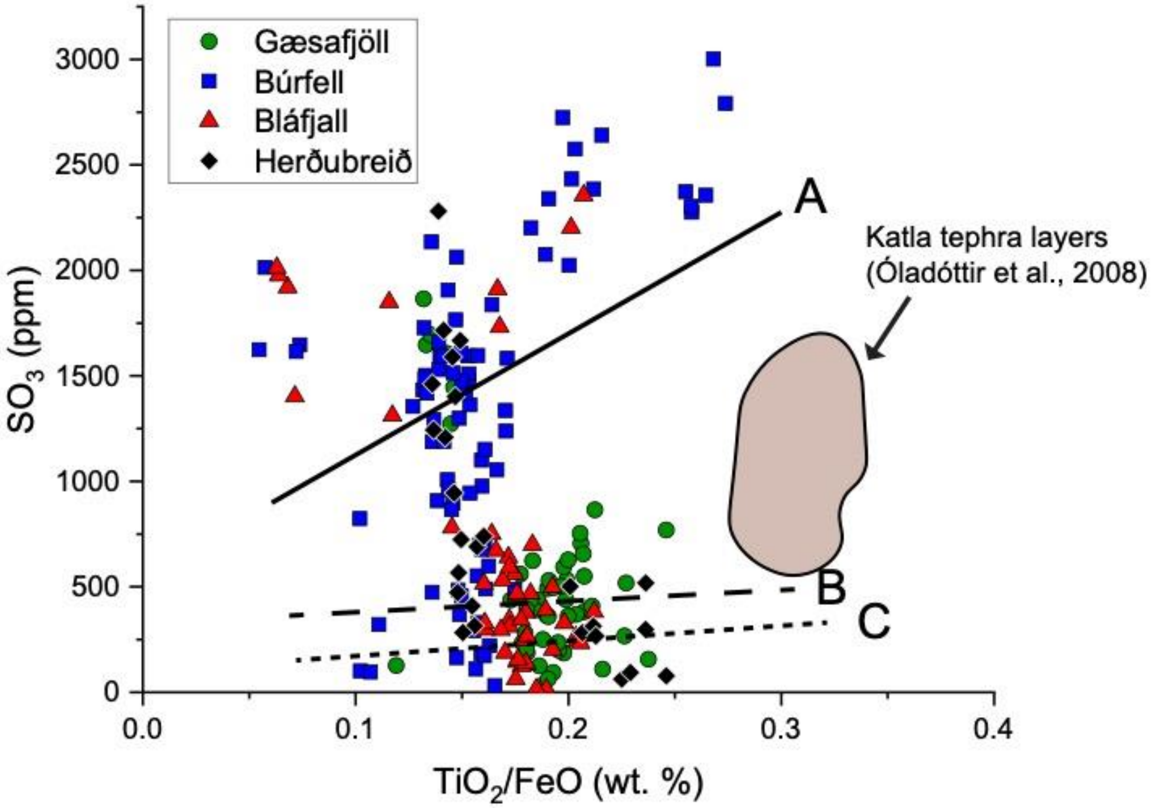

Fig. 5: Graph of SO_3 versus TiO_2/FeO to evaluate sulfur degassing of basaltic glass (Oladottir et al., 2008). Best-fit regression lines for (A) melt inclusions, (B) magmatic tephra, and (C) crystalline lava. Katla tephra layers are outlined in the light brown blob for reference.

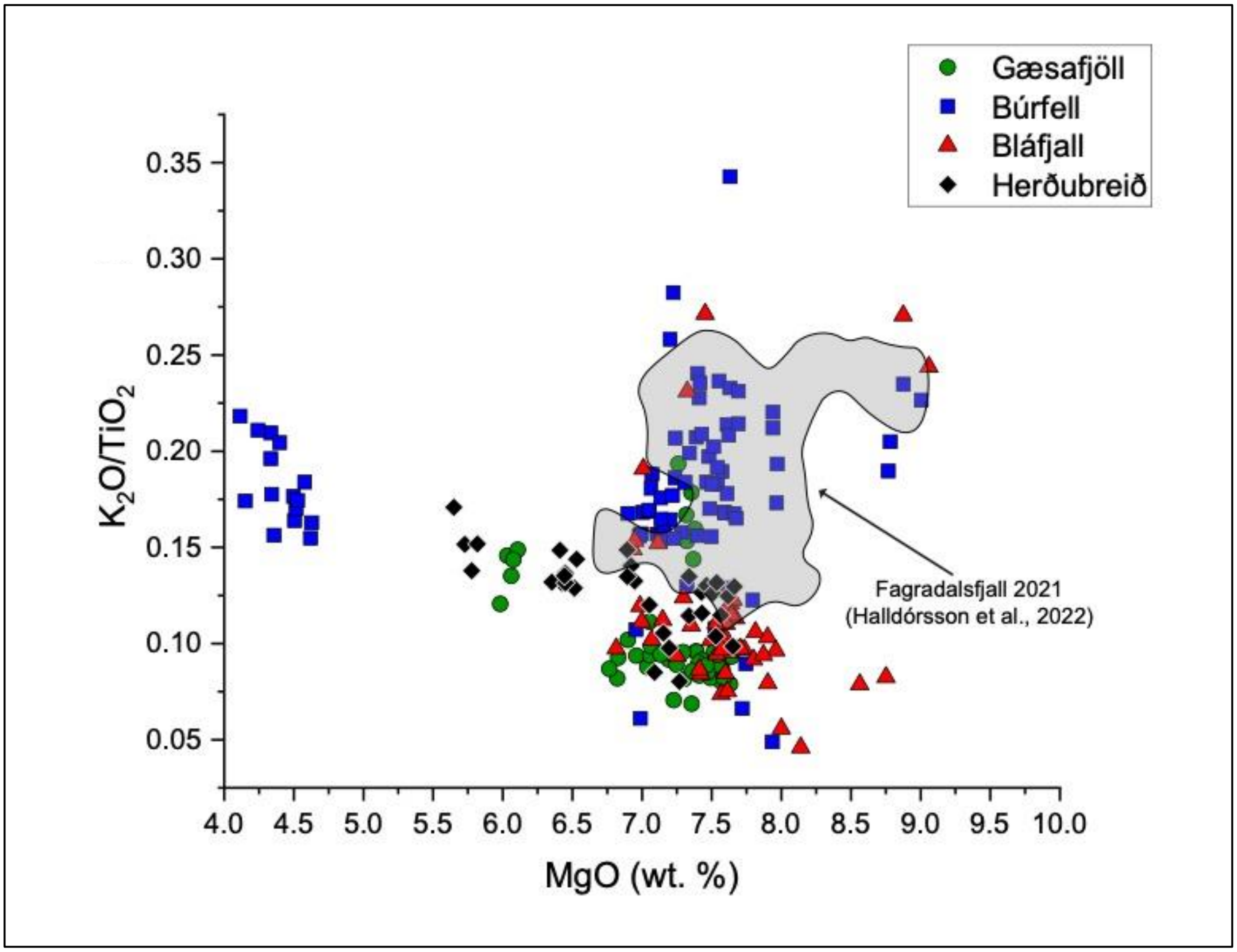

Fig. 6: K_2O/TiO_2 vs. MgO for northeast Iceland tuya glass compared to Fagradalsfjall lavas in 2021 (Halldórsson et al., 2022).

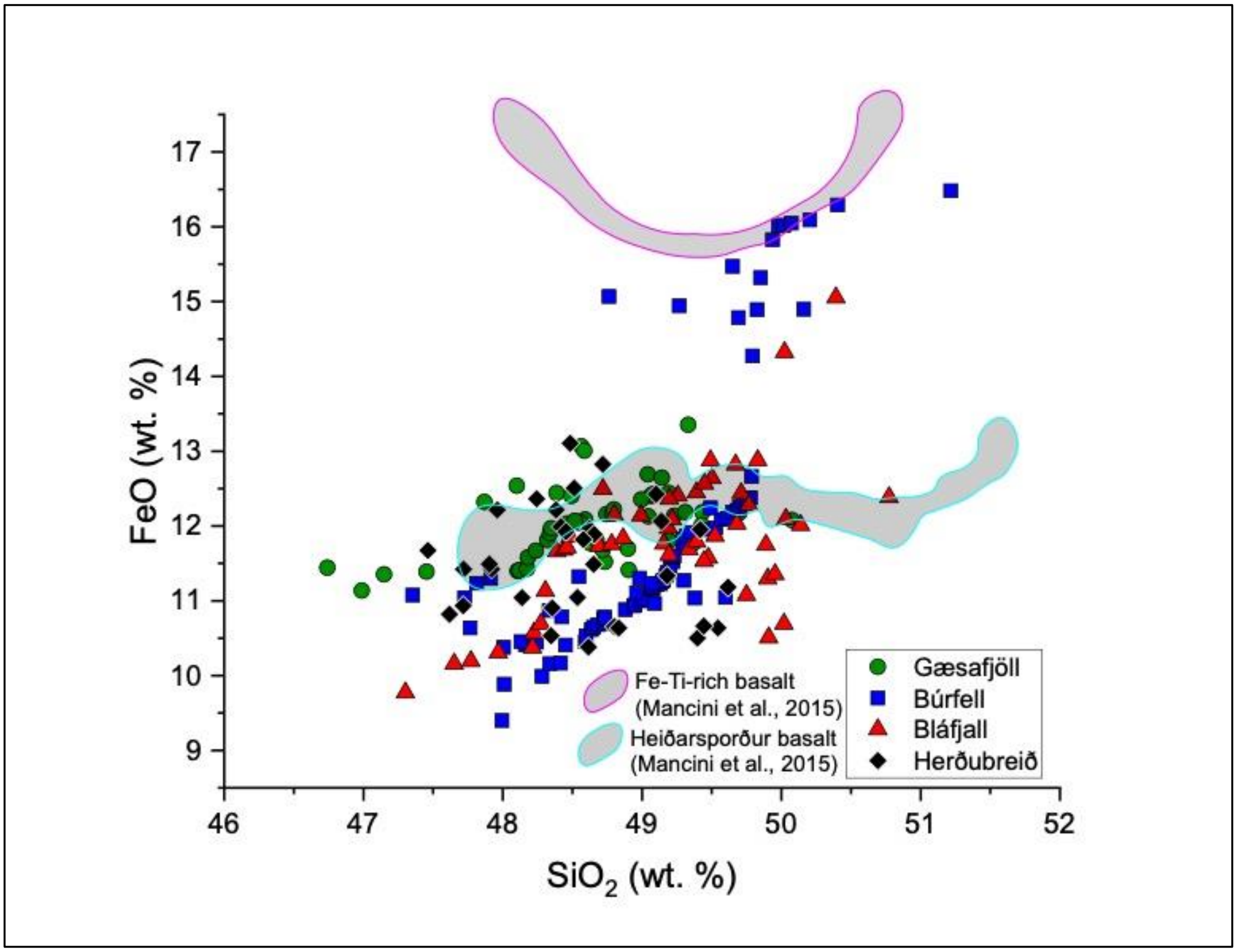

Fig. 7: FeO vs. SiO$_2$ compared to basalts that erupted at Heiðarsporður ridge in northeast Iceland (Mancini et al., 2015).

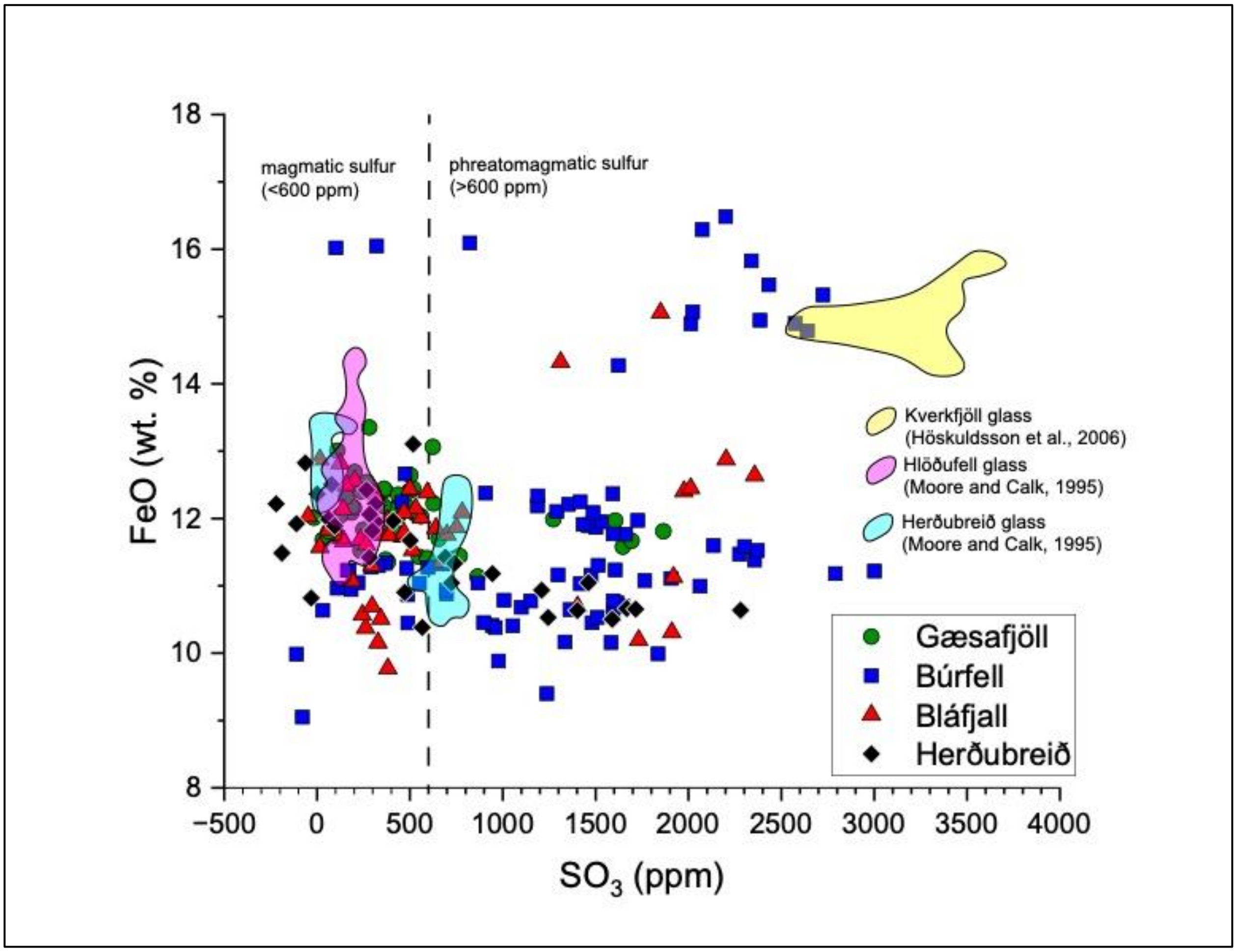

Fig. 8: FeO vs. SO_3 for northeast Iceland glass compared with previous data from Herðubreið, Hlöðufell, and Kverkfjöll. Dashed line at SO_3 600 pm separates magmatic vs. phreatomagmatic sulfur, and may indicate interaction with meltwater (Oladottir et al., 2007).

3.2 H_2O Content Using FTIR

Water content was obtained to look at the volatile evolution of the northeast Iceland tuya glasses. Water content was paired with the sample elevation, manometry water content, and ice thickness estimates. Out of the four tuyas, water content was highest for Búrfell (mean of 0.236 wt.%) and lowest for Gæsafjöll (0.036 wt.%) (Fig. 9). Bláfjall and Herðubreið have the same mean water content of 0.102 wt.% (Fig. 9). For sample elevation, Herðubreið and Bláfjall had the widest range of elevation change compared to Búrfell and Gæsafjöll, and generally their water content decreases when elevation increases, except for Búrfell which remains relatively constant (Fig. 10). For the manometry vs. FTIR water comparsion, most of the sample points plot across the 1:1 line with higher manometric water content than FTIR water, with one exception of Búrfell having higher FTIR water than manometry and one sample of Herðubreið plotting on the 1:1 line (Fig. 11). Only Búrfell has higher FTIR water than manometry, and the rest of the tuyas have higher manometric water, with one sample of Bláfjall having the highest manometric water. Lastly, ice thickness estimates were calculated using VolatileCalc for Búrfell, Bláfjall, and Herðubreið (Fig. 12) (Newman and Lowenstern, 2002). Using an estimated CO_2 content, ice thickness estimates would increase as CO_2 increased, with as much as ~700 m of ice with only 20 ppm of CO_2 (for Búrfell). Búrfell had the highest water contents, therefore the highest ice thickness estimates and Gæsafjöll had the lowest water contents and so the were not able to be calculated due to VolatileCalc requiring at least 0.08 wt.% H_2O when making calculations. Even though Búrfell is the third tallest tuya and third closest south from Vatnajökull glacier out of the four, it still has the highest ice thickness estimates compared to Bláfjall (second tallest; second closest south) and Herðubreið (tallest and closest to Vatnajökull).

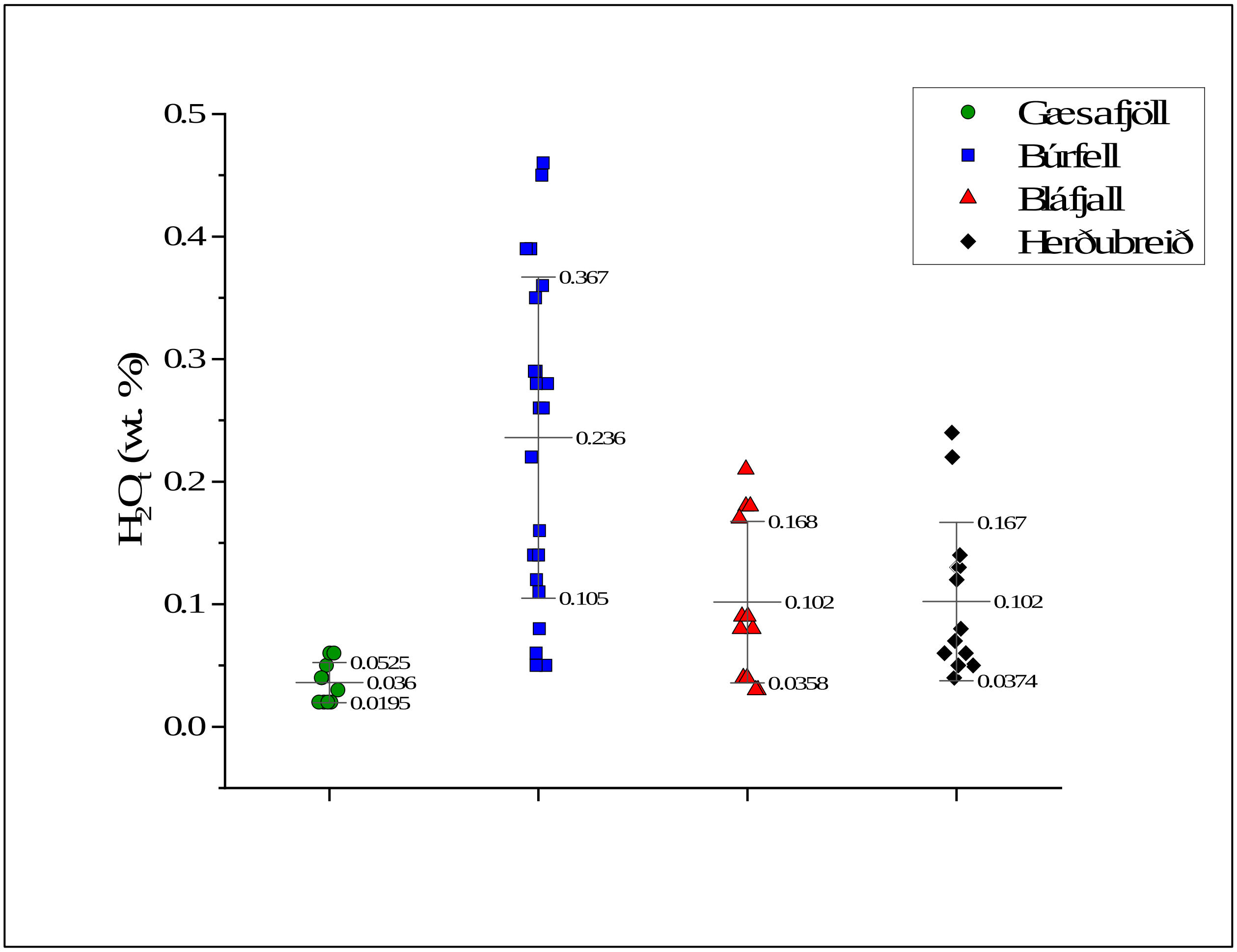

Fig. 9: FTIR water content for all four tuyas; line bars indicate ±1 standard deviation from the mean.

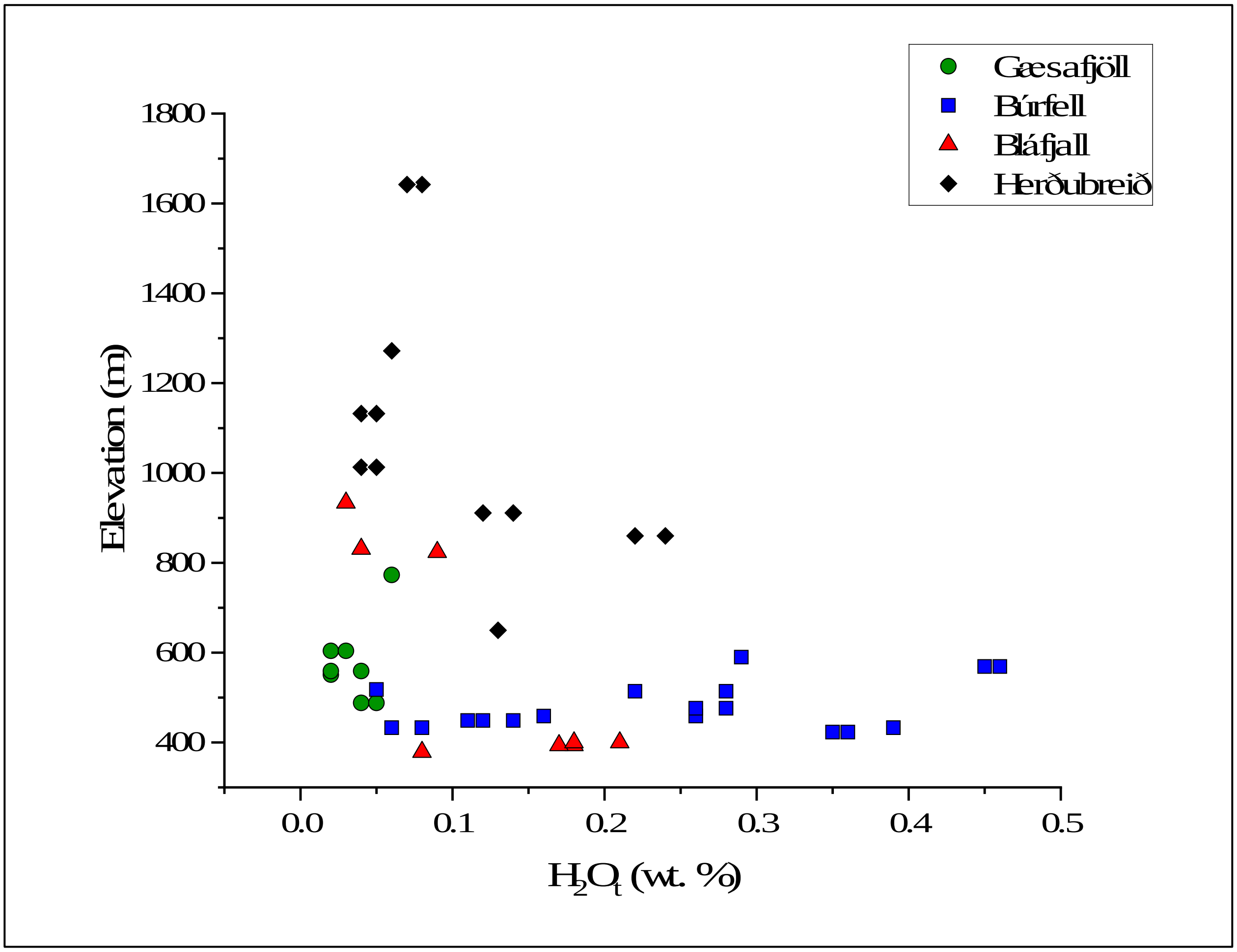

Fig. 10: H_2O_t vs. elevation suggests degassing as water content should decrease with elevation for degassing to have taken place so ice thickness estimates can be calculated.

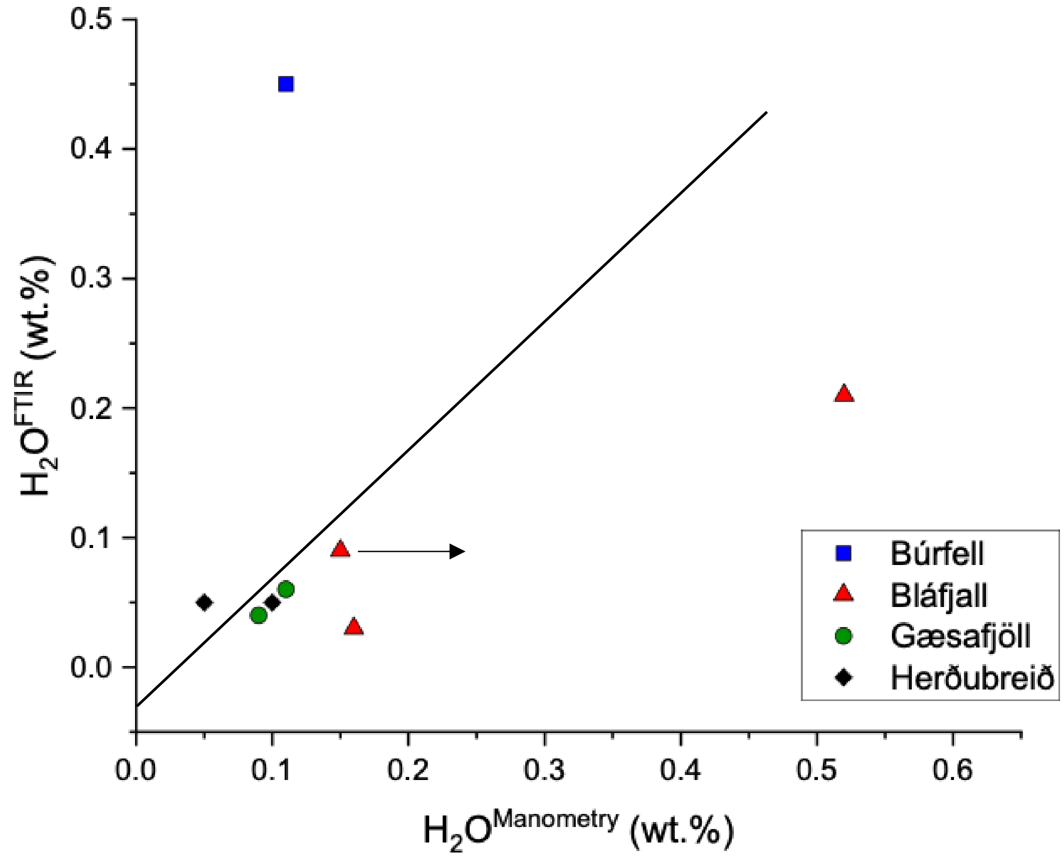

Fig. 11: FTIR and manometry H_2O data for individual tuyas. Black line shows the FTIR and manometry 1:1 ratio; black arrow shows the trend for the tuya glasses. Overall, the FTIR method gave slightly lower contents than the manometric measurements likely because crystal-rich nature of the glass chips was not a significant component of altering the water content to produce high measurements.

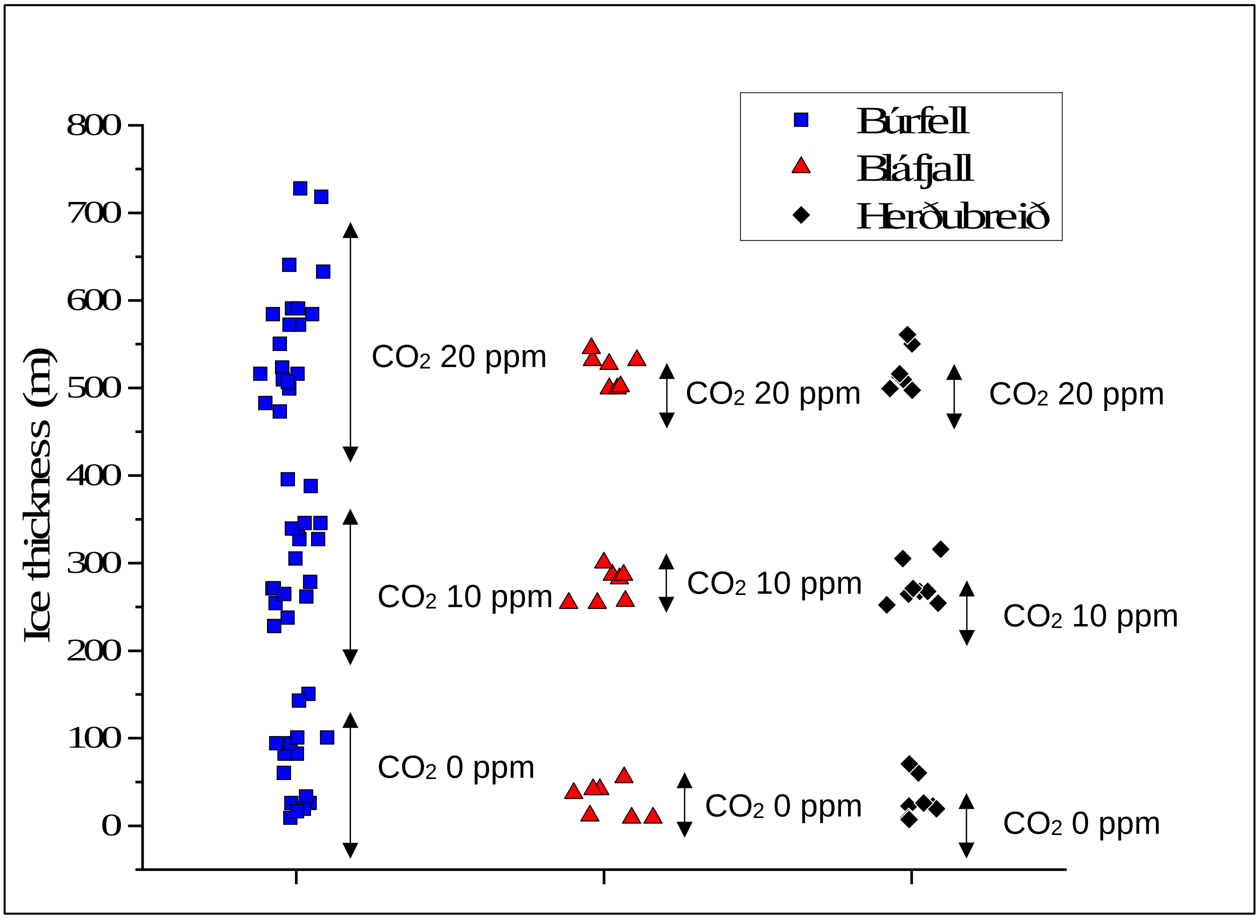

Fig. 12: Ice thickness estimates using VolatileCalc (Newman and Lowenstern, 2002) software for three of the four tuyas in northeast Iceland. CO_2 was also estimated during calculations and show an increase in ice thickness as CO_2 increases.

3.3 H_2O Content and Hydrogen Isotopes Using Manometry

3.3.1 δD vs. H_2O_t

Table 2 reports the δD and H_2O contents determined by manometry. δD (hydrogen isotopes) vs. H_2O_t shows how the water content and hydrogen isotopes of the glass varies for each of the four tuyas during syn-eruptive events (Fig. 13, 14). A total of eight analyses were collected: Gæsafjöll has two analyses of water contents at 0.09 and 0.11 wt. % and δD at –101 ‰ for both analyses; Búrfell has one data point at 0.11 wt. % H_2O_t and δD at –105 ‰; Bláfjall has water contents at 0.16–0.52 wt. % and δD –49 to –108 ‰; Herðubreið has two data points with water content at 0.05 wt. % and 0.10 wt. % and δD at –87 ‰ and –101 ‰.

Overall, Bláfjall shows the widest range of values for water content and δD, followed by Herðubreið, then Gæsafjöll, and then Búrfell. Bláfjall has both the highest water content and the highest δD content. All samples had water contents <0.25 wt. % and δD contents between –85 and –110‰, with only one point of Bláfjall's high-water content and high δD value (0.52 wt. %; –49 ‰). Both Gæsafjöll and the one data point of Búrfell show some of the lower water contents and δD values, with one data point of Bláfjall having the lowest water content and δD value. Gæsafjöll does not appear to show a trend of increasing δD with increasing water content that is shown for Herðubreið and Bláfjall, and it is also hard to tell if this trend would occur since there is only one data point of Búrfell.

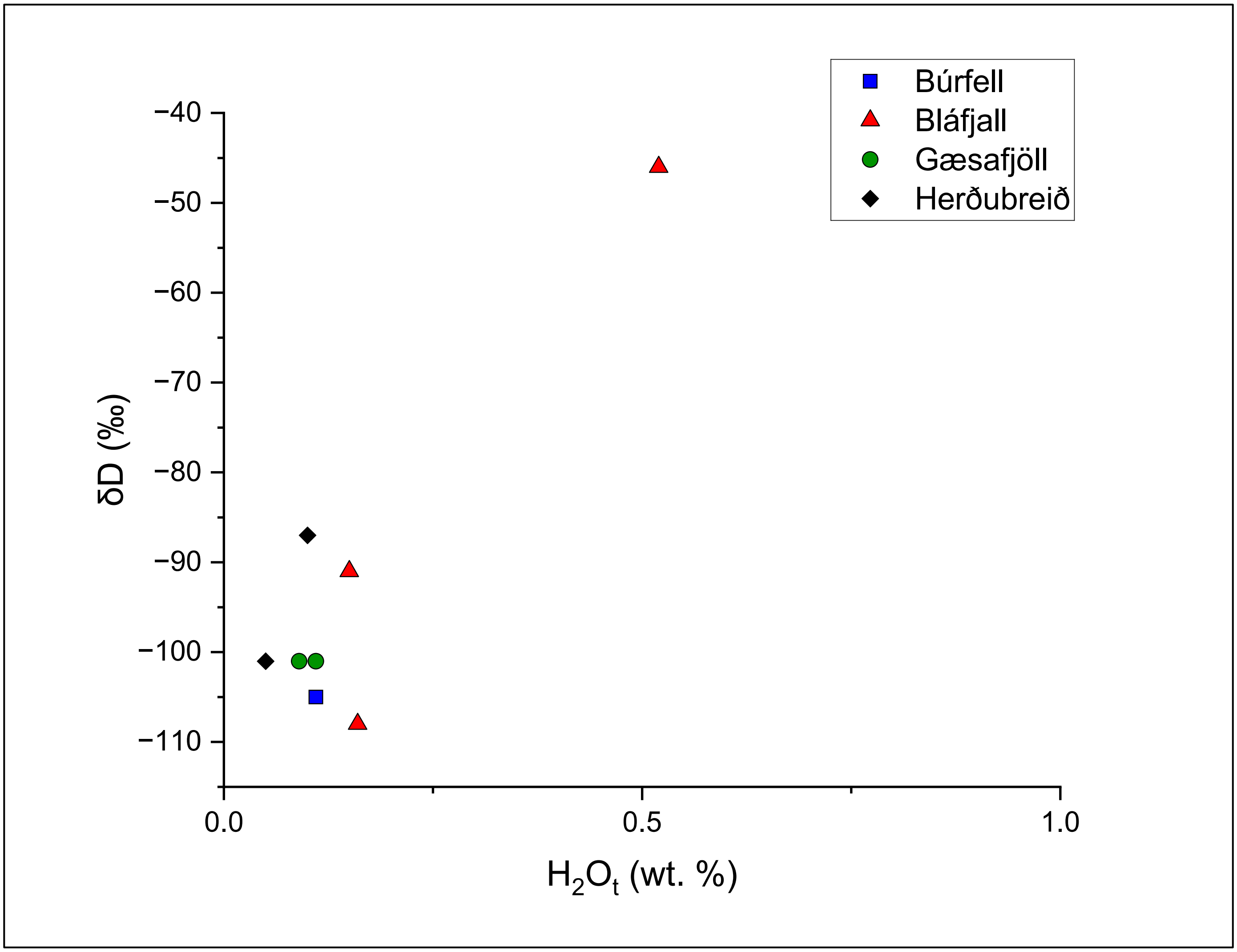

Fig. 13: δD (hydrogen isotopes) and H_2O_t content for all tuyas; these data suggest open versus closed system processes (DeGroat et al., 2002). A closed system would reflect a sealed magma chamber whereby an eruption does not interact with its surrounding environment during its ascent to the surface, and no volatiles enter or leave the system. An open system would be magma that exchanges volatiles with their environment and can flow across boundaries with its environment.

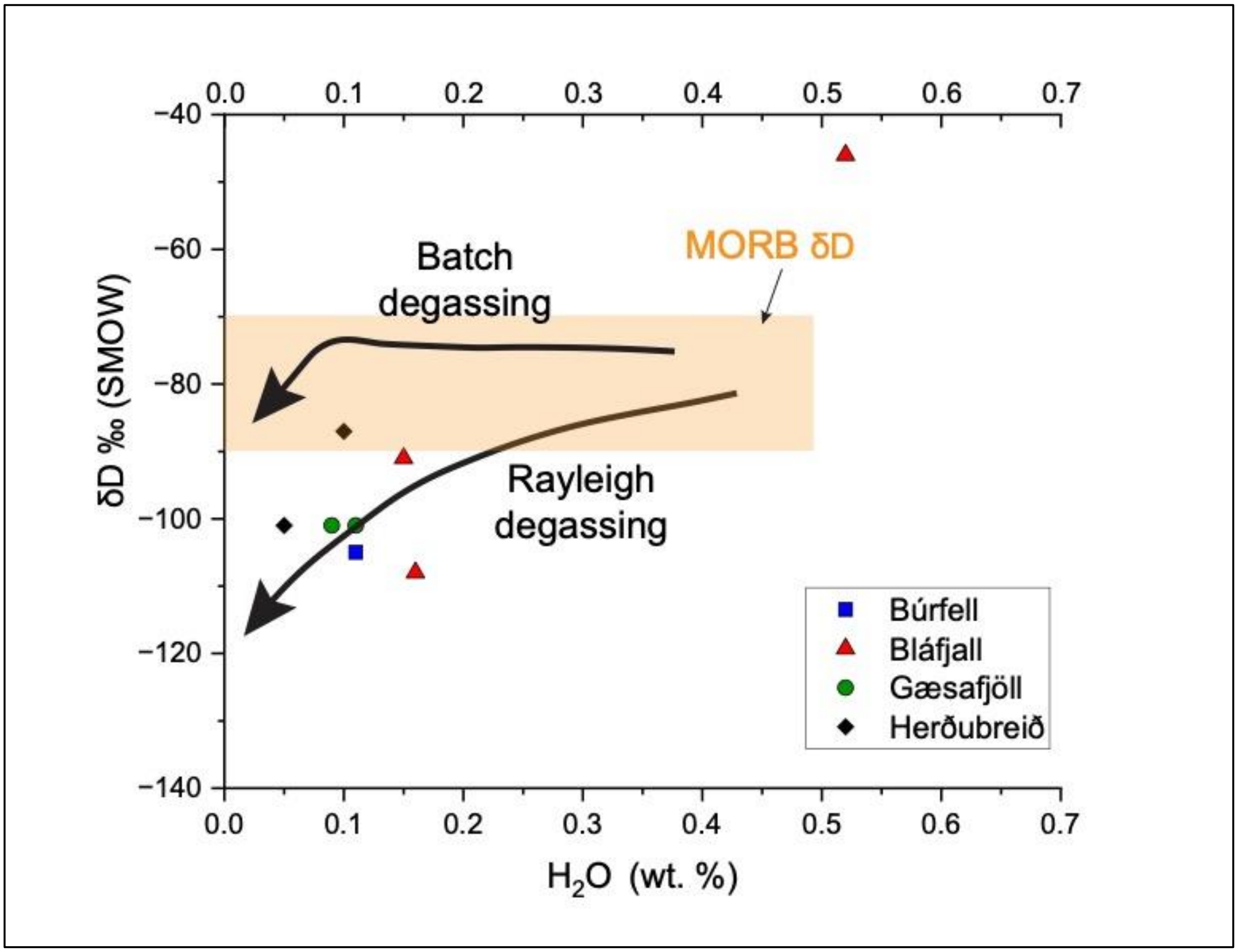

Fig. 14: δD-H_2O variation in glasses from northeast Iceland tuyas compared to the range of fresh MORB (Dixon et al., 2017). The mild decrease in δD observed in some of the northeast Iceland glasses is likely due to near-surface degassing (Batch and Rayleigh degassing curves shown for degassing mechanisms).

Table 2. Manometry Data

Sample Name	δD (‰)	repeat	Water(wt.%)
BF23-02 G	-105		0.11
BL22-06 G	-46	-45	0.52
BL23-03 G	-91		0.15
BL23-06 G	-108		0.16
GS23-04 G	-101		0.09
GS23-05 G	-101		0.11
HE23-05 G	-87		0.10
HE23-06B G	-101		0.05

4. Discussion

4.1 Magma Evolution and Meltwater Interaction

The two different compositions of basaltic glass show possibilities for magma evolution in the area: (1) different mantle sources (Halldórsson et al., 2022) or (2) an extended eruptive period (Halldórsson et al., 2022). Magma evolution typically occurs related to important magmatic process such as crystal fractionation, magma mixing, crustal assimilation, or liquid immiscibility. For crystal fractionation, olivine and plagioclase fractionation did not occur, due to a positive relationship as MgO and CaO increase as SiO_2 increases (except for Herðubreið for CaO) (Fig. 3a–h). Gæsafjöll and Bláfjall have similar major element concentrations, whereas Búrfell exhibits a magma componentenriched in FeO, and this group is also depleted in MgO and CaO. This Fe-rich magma type may be a common occurrence in northeast Iceland (Mancini et al., 2015). The higher MgO and lower FeO component resembles olivine-basalt and the low MgO and higher FeO component is in line with Fe-Ti basalts at Krafla and Heiðarsporður ridge. At Heiðarsporður ridge, the trends of the Fe-Ti basalts were explained by crystal fractionation of pyroxene prior to Fe-Ti oxide stability in more evolved magmas, which is in line with Herðubreið but not the other for tuyas (Fig. 3b; Mancini et al., 2015). In addtion, magma mixing may have been an improtant part to magma evolution in the region due to the distribution of mantle sources (Fig. 6). The high-MgO and high K_2O/TiO_2 component of Búrfell mostly overlaps the recent Fagradalsfjall eruptions on the Rekyjanes peninsula, suggesting involvement of enriched mantle source regions. However, lower MgO components for Búrfell are also common, as well as less prominent but still notable for Gæsafjöll and Herðubreið, suggesting distinct magma batches from shallow, more depleted mantle sources (Halldórsson et al., 2022).

Furthermore, Búrfell lacks the dacites common at Heiðarsporður ridge, which is important because Heiðarsporður is in close proximity to Búrfell (1–2 km), and how the composition of eruptive products changes drastically over short spatial scales. Yet Búrfell may have more evolved magma in the subsurface that is not eruptible due to viscosity (Mancini et al., 2015). Low viscosity mafic magma may extract minerals entrained in the crystal mush stored in a tiered sill-like magma reservoir to form the Fe-Ti basalts during mafic recharge (Fig. 7; Mancini et al., 2015), Thus, we infer similar processes occurred at Búrfell and Bláfjall tuyas to generate the Fe-Ti basalts. On the other hand, Gæsafjöll, one of the tuyas in this study closest to Búrfell, also has rhyolitic domes associated with its formation. Zircon ages from the domes of Gæsafjöll reveal the age to be 85.5±9.4 ka. The Lúdent fires, near Búrfell, formed Heiðarsporður ridge and are suggested to start ca. 9,000 ka. This makes sense considering the formation of Búrfell may have coincided with glacial unloading at the onset of deglaciation with a similar magma composition to Heiðarsporður (Fig. 7), but it is unclear if Gæsafjöll was connected to this event as well given the older age of its rhyolite dome.

Furthermore, Fe-Ti basalt trends are also recorded in other volcanic zones in Iceland. For example, Katla, a volcano under the Mýrdalsjökull ice cap, has a bimodal magma distribution that is similar to Gæsafjöll: Fe-Ti transitional alkali basalts and mildly alkalic rhyolites (Lacasse et al., 2007). Based on this distribution, one suggestion for the formation of Gæsafjöll is magma mixing (Lacasse et al., 2007); however, little to no compositional heterogeneities (i.e., enclaves for magma mixing) are preserved in the sub-aerial lava flows based on thin section analyses, but compositional heterogeneities based on major elements and volatiles may be present at Gæsafjöll (Fig. 4, 6). This may be due to the longer time scale differences based on the older age of the rhyolites at Gæsafjöll compared to the younger subaerial lavas that cap the tuya. It has been suggested in Iceland that it takes ~100 Ma for rhyolites to form (Banik et al., 2018), and so this leaves time for mafic recharge to mix with silicic melts in progress. Partial melting of the mantle and magma upwelling of hot, less viscous basaltic magma has been one idea for triggering an eruption; however, little research has been done if rhyolites can trigger basaltic eruptions (Eichelberger et al., 2006). In the case of Gæsafjöll, the rhyolite domes were the first to erupt generated by fractional crystallization of basaltic magmas (Hampton et al., 2021) that pond into different pockets of magma reservoirs for silicic magmas. On the other hand, not too far away from Gæsafjöll, Bláfjall tuya has been suggested to also form by partial melting of the upper mantle, but secondary magma reservoirs and gabbroic cumulates dominate this area of the crust (Schiellerup et al., 1995). Therefore, magmatic plumbing systems in northeast Iceland may resemble tiered sill-like bodies which has been previously proposed in other areas of Iceland such as the Reykjanes peninsula (Caracciolo et al., 2023). Glass geochemistry suggests that secondary magma reservoirs may be common for this area (Schiellerup et al., 1995), and so the compositional differences between the proximal tuyas may—albeit slight—be explained by the northern volcanic zone being subdivided into fissure swarms (Hjartardóttir et al., 2012). Another situation to explain this difference would be the timing of eruptions based on cosmogenic ages, and more time for crystallization of different reservoirs for changes in composition, as recorded for some glass chips at Bláfjall (Schiellerup et al., 1995). This is also shown in Fig. 3d and Fig. 3e with Bláfjall glass having a slightly more evolved composition compared to Gæsafjöll glass.

For the generation of different rock types at Gæsafjöll, there may have been uneruptible, viscous magma at Gæsafjöll during a glaciated period, and then perhaps deglaciation caused decompression melting in the mantle to produe new basaltic magmas (de Vries et al., 2018). Other tuyas in the western volcanic zone of Iceland near one of Iceland's moderately large glaciers, Langjökull, have also experienced this deglaciation effect for prompting new magma generation (Eason et al., 2015). Anomalously high volcanic production rates coincide with higher CaO and SiO_2 and lower FeO at a given MgO in this region of Iceland (Eason et al., 2015).

Sulfur can be used as a proxy for water in magmatic systems sharing a volatile nature. Slfur content tends to not drop below 600 ppm with ice-covered volcanoes such as Katla (Oladottir et al., 2007), which is inferred to be phreatomagmatic sulfur compared to magmatic sulfur (<600 ppm). Lower SO_3 concentrations (<600 ppm) suggest more degassed magma erupted under very thin ice or subaerially, whereas higher concentrations (>600 ppm) suggest undegassed magma erupted beneath thicker ice (Fig. 8). So, the glass generated may have formed during complex eruptive events representing different degrees of degassing under disparate ice conditions. For this study, sulfur spans a whole range from 0–3,000 ppm, which suggests that there were magmatic eruptions where efficient sulfur degassing was taking place to become depleted (<600 ppm phase). Then there were glacio-volcanic eruptive phases, which limited sulfur degassing leading to higher sulfur contents (>600 ppm).

The Lúdent fires occurred around the same time Búrfell formed, and they may have originated from the same magma source, but the Lúdent fires do not record any interaction with meltwater or ice with the formation of hyaloclastites and pillow basalts. If Búrfell is connected to Heiðarsporður at all, then that would mean deglaciation took place during a time span of ca. 1.8±0.3 ka (10.8±0.3 ka (-) 9.0 ka) since Heiðarsporður is not suggested to interact with ice or meltwater (Mancini et al., 2015). Glass SO_3 contents, which is a volatile element like water, range between 100 ppm and 3,100 ppm for all three edifices with SO_3 contents generally increasing towards the south based on their means (Fig. 4). Therefore, phreatomagmatic processes dominate in northeast Iceland as tuyas progress toward Vatnajökull glacier (Fig. 4, 8); however, Búrfell contains the highest mean which suggests the most interaction with water/ice compared to the other three tuyas, even exceeding Herðubreið which is the tuya furthest south and closest to Vatnajökull glacier.

Furthermore, TiO_2/FeO^* paired with SO_3 can be used to determine if the glass is more similar to contents from undegassed melt inclusions, degassed magmatic tephra, or degassed crystalline lava (Fig. 5; Óladottir et al., 2007). This affirms the overall phreatomagmatic origin of the volcanic glasses. Many of the tuya glasses plot at or above undegassed melt inclusion (A) values, whereas another group of glasses plot between melt inclusions (A) and magmatic tephra (B) lines and represent partially degassed phreatomagmatic magmas (Fig. 5; Óladottir et al., 2007). The TiO_2/FeO^* content is variable for all four tuyas compared to Katla (~$TiO_2/FeO^*=0.30$) values likely because some of the higher FeO glasses would have lower TiO_2/FeO^*.

4.2 Using Volatiles to Understand Degassing Mechanisms

δD vs. H_2O is useful in decoding open and closed system processes of the magma chamber (Taylor et al., 1983; DeGroat et al., 2002). Except for one Herðubreið sample, the northeast Iceland tuya glasses do not overlap the global Mid-Ocean Ridge Basalt (MORB) values of –80 ± 10‰. One hydrous sample of Bláfjall falls beneath the Rayleigh (open system) degassing trend

(Fig. 13, 14). The samples have low water contents and therefore are less hydrous than MORB, which typically have water contents of 0.2–0.6 wt.% (Dixon et al., 2017). Degassing leads to a decrease in water content and δD value. If degassing from a primary magma with 0.6 wt.% H_2O is incremental (continuous depletion in δD and low water contents) and of the Rayleigh type, it can result in a decrease of up to 20–30‰ in the δD value of the residual basaltic glass (De Hoog et al., 2001), but only a change of 10‰ would be of the Batch-type or closed system degassing (Taylor et al., 1983). Given a starting composition of the University of Oregon basalt glass standard (Bindemann et al., 2021), it is likely that Rayleigh degassing mechanisms occurred for the tuyas in northeast Iceland. Hence, the low water content and depleted δD values suggest that substantial amounts of water have been lost during degassing from prolonged eruption under ice, which may imply that the measured δD values are not those of the original, undegassed parental magmas due to open system processes (De Hoog et al., 2009).

4.3 Reconstructing Ice thickness Using Water Content

Water and carbon dioxide concentrations can be used to calculate ice thickness (Dixon et al., 2002; Höskuldsson et al., 2006; Owen et al., 2018); however, five criteria must be met prior to making these calculations (Tuffen et al., 2010): (1) volatile saturation has been reached; (2) degassing was in equilibrium; (3) homogenous samples are present; (4) no post-quenching movement or change in elevation present; (5) no post quenching hydration present. The guidelines for each of the criteria follows: (1) The presence of vesicles indicates that some degassing has taken place and therefore the point of volatile saturation must have been reached (Tuffen et al., 2010; Höskuldsson et al., 2006). Alternatively, a negative relationship between elevation and water content is also evidence that degassing has taken place (Dixon et al., 2002); (2) equilibrium degassing should be achieved if the ascent rate was $< 0.7\ \mathrm{ms}^{-1}$ (Rutherford et al., 2008); (3) avoidance of complex textures and similarity between analysis of multiple data points within the same sample (Tuffen et al., 2010); (4) field evidence for reworking of glass (Tuffen et al., 2010); (5) perlitisation textures and high molecular water content (Tuffen et al., 2010; Denton et al., 2009; Yokoyama et al., 2008).

For the northeast Iceland samples, some criteria were met, some have not been evaluated yet, and some were not met. First, tuyas glasses are vesicular. Moreover, three of the four tuyas show decreasing water content with elevation: Gæsafjöll, Bláfjall, and Herðubreið, with one outlier for Gæsafjöll of the high water content at high elevation (Fig. 10), though most of the glasses have vesicles suggesting saturation. However, Búrfell has an increase in water content with elevation, and therefore would not qualify for criterion (1). Second, eruption models for these four tuyas in northeast Iceland have not been done yet, and therefore their ascent rate remains unknown , and δD isotopes and water content show open system degassing is the dominate process for one of the eruption mechanisms, which suggests their degassing remained in disequilibrium throughout its ascent rate, with one outlier for Bláfjall. Next, three of the four tuyas had homogenous samples for their H_2O_t content: Gæsafjöll, Bláfjall, and Herðubreið; however, Búrfell did not have homogenous H_2O_t content (Appendix C). During analysis, the sample thickness of the glass needs to be ideally ca. 100 µm in order to perform accurate FTIR analysis; these data of high water content for Búrfell (0.77–1.64 wt. %) needed to be reanaylzed due to the glass wafers being too thick. Once reanlayzed, these samples yielded a lower water contents (0.22–0.36 wt. %). Thus, Búrfell does not meet criterion (3), but Gæsafjöll, Bláfjall, and Herðubreið do. Lastly, two out of the four tuyas show evidence of post-quenching movement: Búrfell and Bláfjall. For Búrfell, seven samples were collected on a slumped hyaloclastite/pillow basalt ridge near Búrfell, so these samples reflect a glacio-volcanic ridge connected to the tuya. In addition, four samples (two analyzed by FTIR: BL2206 and BL2204) were collected at Bláfjallsfjallgarður, which is a separate ridge that may be connected to Bláfjall (Sigurbergsdóttir et al., 2023) but is not a part of the main Bláfjall edifice.

Saturation pressures for basalt magmas were determined using the software VolatileCalc to estimate ice thicknesses (Fig. 12) (Newman and Lowenstern, 2002). Saturation pressures for Gæsafjöll were not calculated due to low water contents since the software needs at least 0.08 wt. % H_2O.. One reason Gæsafjöll's water contents are so low is due to the magma being extremely degassed during eruption. The other three tuyas were less degassed and had sufficient water contents for an ice thickness estimate. CO_2 is an importantvolatile in magmas, but FTIR measurements show no CO_2 peaks were observed indicating CO_2 concentrations were below detection limit (~30 ppm), and so CO_2 is estimated for ice thickness measurements as well. CO_2 exsolves at much deeper depths than either water or sulfur and consequently often has very low concentrations in glacio-volcanic glasses.

Ice thickness estimates are highest for Búrfell (9–728 m) and lower for Herðubreið (7–561 m) and Bláfjall (9–545 m). Estimated ice thicknesses for the four tuyas are substantially lower than ~1.5 km reported for Kverkfjöll near Vatnajökull glacier (Höskuldsson et al. 2006). Interestingly, Sigurbergsdóttir (2023) suggested the ice thickness at Bláfjall was about 700 m and thinned northward, in line with our estimates assuming 20 ppm CO_2 for Búrfell. Therefore, ice thickness estimates for northeast Iceland may not have increased to the south towards Vatnajökull glacier as previously thought (Walker, 1965; Licciardi et al., 2008). There may have been thicker ice to the north during the end of the Pleistocene for Búrfell and Herðubreið since they erupted around the same time (Licciardi et al., 2008). For Bláfjall and Gæsafjöll, Bláfjall may have moderate ice thicknesses towards the south, and Gæsafjöll may have had thin ice or meltwater interaction to yield low water contents. This suggests that during an older period of the Pleistocene (14.4±1.0 ka; Licciardi et al., 2008) had a warmer, less extensive ice sheet compared to Búrfell and Herðubreið.

Overall, using volcanic glass to help estimate ice thickness in northeast Iceland should be treated with caution. Without accurate CO_2 measurements in the volcanic glass, ice thickness estimates can vary widely from very thin to very thick ice. Eruptions under glaciers can vary if they are under thin versus thick ice, and therefore an accurate quantification of their previous thickness is crucial, and these data can become speculative for their previous paleoenvironmental formation. Furthermore, a continuous section of sampling from low to high elevation of the tuya should be achieved to show that progressive degassing has taken place using volatile analysis. However, the conceptual model shows that ice thickness estimates using sulfur content and water content show a similar trend, with increasing sulfur with increasing water content suggesting more water interaction and possibly thicker ice (Fig. 15). In the end, volcanic glass forms from rapidly cooled lava, and therefore suggests some ice or water component for their tuya formation and provides a snapshot of when the volcanic glass quenched under a certain pressure, whether it be ice or meltwater. With our new results, the hypothesis that ice thickness increased to the south towards Vatnajökull glacier may be more complex than previously thought by Walker, 1965 and using tuyas for paleoenvironmental reconstructions should not only use the elevation of their glacio-volcanic deposits, but accurate volatile measurements as well. Some recommendations also include preparing adequate sample mounts for accurate water content analysis and field sampling of glass that are not re-worked or re-hydrated.

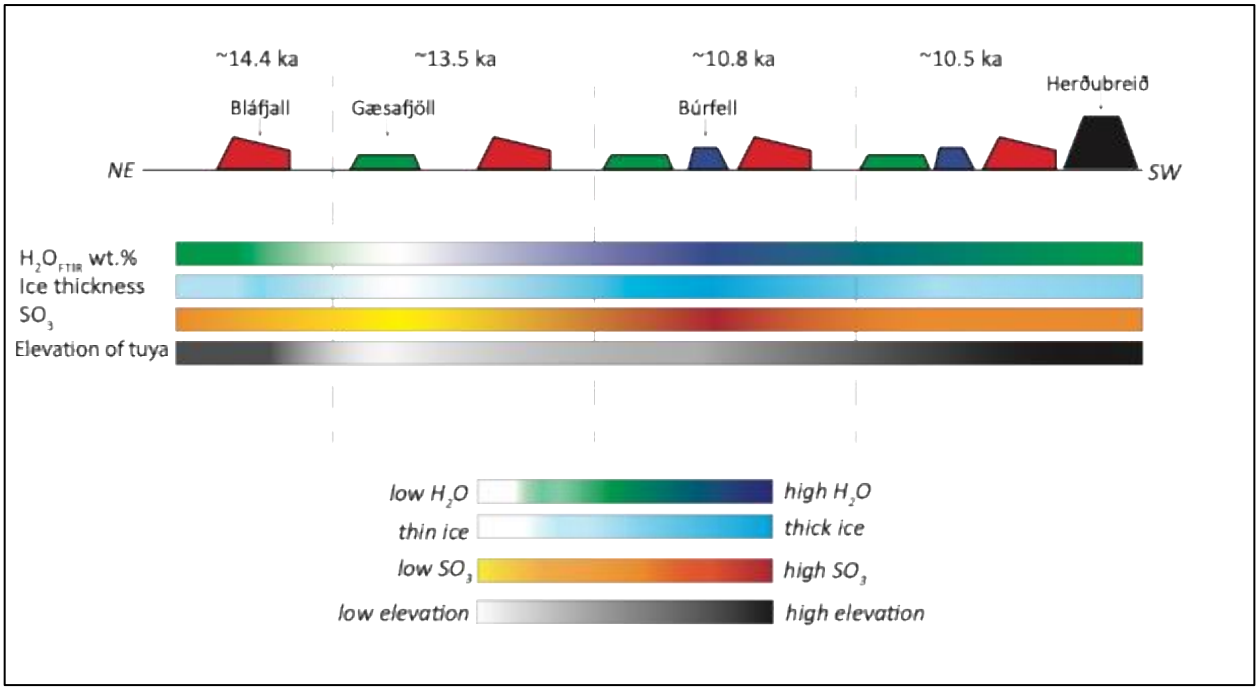

Fig. 15: Conceptual model for northeast Iceland tuya formation from ~14.4 ka to ~10.5 ka based on previous cosmogenic ages (Licciardi et al., 2007). Bláfjall formed first, then Gæsafjöll, Búrfell, and finally Herðubreið. The gradient legend shows how each of the four main datasets collected on the paleoenvironment for northeast Iceland have evolved through time.

5. Conclusions

Overall, three conclusions can be drawn from using volcanic glass as a paleoenvironmental indicator and to help understand eruption mechanisms:

1. Glacio-volcanic/phreatomagmatic processes dominate in northeast Iceland as tuyas progress toward Vatnajökull glacier based on SO_3 concentrations. The increase in SO_3 content as the tuyas reach Vatnajökull is inferred to be the result of eruptions into thicker ice, with the thinnest ice at Gæsafjöll and the thickest ice at Bláfjall. However, a separate component of Búrfell glasses is in line with previous data at Kverkfjöll, the tuya

closest to Vatnajökull and where the thickest ice might be postulated. This poses more questions on the simple hypothesis of coeval eruptions with an increase in ice thickness towards Vatnajökull and raises the possibility of eruptions at different glacial stages with varying ice thickness.

2. H_2O content using FTIR should be used with caution when estimating ice thickness, and make sure the five criteria for ice thickness estimates should be met (Tuffen et al., 2010). However, preliminary results of H_2O content show that Búrfell has the highest H_2O content compared to Gæsafjöll, Bláfjall, and Herðubreið, which suggested Búrfell erupted under thicker ice and the other three tuyas erupted under thinner ice. Therefore, the previous hypothesis that there was thicker ice for tuyas in northeast Iceland that erupted more proximal to Vatnajökull ice cap may be not as simple as previously hypothesized, with varying ice thicknesses across northeast Iceland at different times in the Pleistocene. In addition, these are some of the first ice thickness estimates for northeast Iceland using volcanic glass analyses. Previous work utilizing marine sediments and glacial features to understand the extent of the Iceland ice sheet during the Pleistocene can now be quantified because previous research has focused on the extent of the ice sheet and not the thickness (Patton et al., 2017; Benediktsson et al., 2023).
3. Hydrogen isotopes can vary extensively since any modification from depth to surface can alter its isotopic composition (Sharp, 2017). Hydrogen isotope and water contents determined by manometry suggest open vs. closed system processes during eruption and approximate Raleigh degassing curve, which suggests an open system was the

dominant mechanism during magma ascent. An open system implies exsolved volatiles are lost from contact with the magma, and accordingly, the volatiles quenched and recorded in the volcanic glass may not have been the original volatile content since post eruption slumping could confuse the *in situ* or in place ice thickness because degassed magma might slump to lower elevation and then based on the water content, the deposits should have erupted at a higher elevation (i.e., low water content at the base of the tuya rather than closer to the top). Ultimately, the degassed magmas do interact with the overlying ice and record an ice thickness—despite the slumping—which is recorded by hyaloclastites having more degassing, therefore lower water contents, and thinner ice, whereas pillow basalts have less degassing, higher water content, and thick ice.

Future work should help refine paleoenvironmental reconstructions of tuya eruptions in northeast:

1. Test different dating methods to provide ages of the subaerial basaltic lava flows. Providing ages for basaltic lava flows in Iceland are notoriously difficult due to the low potassium content used for ^{40}Ar/^{39}Ar dating; however, paleomagnetism in Iceland has been used to date Holocene and Pleistocene lava flows with accuracy (Pinton et al., 2018). Furthermore, since some of the potassium contents for the northeast Iceland glass are high enough for ^{40}Ar/^{39}Ar dating, it could therefore provide accurate ages for the tuyas during the Pleistocene; previous work in Iceland using the ^{40}Ar/^{39}Ar method has had some success of dating basaltic rocks/lava flows (Flude et al., 2008).

2. Explore other methods for collecting water content of volcanic glass. The FTIR method has been frequently cited as an arduous process for collecting water content due to the polishing procedure. Polishing samples may take months and may be polished away since samples need to be sufficiently thin for the FTIR to avoid crystals for an accurate measurement of water content in volcanic glass. Therefore, secondary ion mass spectrometry (SIMS) has been used to analyze water content as well, and with more accuracy and less error. Therefore, utilizing multiple or different methods that can reproduce ice thickness estimates in a reproduceable, timely manner is encouraged.

References

Banik, T.J., Miller, C.F., Fisher, C.M., Coble, M.A. and Vervoort, J.D., 2018. Magmatic-tectonic control on the generation of silicic magmas in Iceland: Constraints from Hafnarfjall-Skarðsheiði volcano. *Lithos*, *318*, pp.326-339.

Bas, M.L., Maitre, R.L., Streckeisen, A., Zanettin, B. and IUGS Subcommission on the Systematics of Igneous Rocks, 1986. A chemical classification of volcanic rocks based on the total alkali-silica diagram. *Journal of petrology*, *27*(3), pp.745-750.

Bemmelen, R.W. and Rutten, M.G., 1955. *Table mountains of northern Iceland*. Brill Archive.

Benediktsson, Í.Ö., Brynjólfsson, S. and Ásbjörnsdóttir, L., 2023. Iceland: glacial landforms during deglaciation. In *European Glacial Landscapes* (pp. 149-155). Elsevier.

Bindeman, I.N., Deegan, F.M., Troll, V.R., Thordarson, T., Höskuldsson, Á., Moreland, W.M., Zorn, E.U., Shevchenko, A.V. and Walter, T.R., 2022. Diverse mantle components with invariant oxygen isotopes in the 2021 Fagradalsfjall eruption, Iceland. *Nature Communications*, *13*(1), p.3737.

Breddam, K., 2002. Kistufell: primitive melt from the Iceland mantle plume. *Journal of Petrology*, *43*(2), pp.345-373.

Butler, R.F. and Butler, R.F., 1992. *Paleomagnetism: magnetic domains to geologic terranes* (Vol. 319). Boston: Blackwell Scientific Publications.

Carley, T.L., Miller, C.F., Wooden, J.L., Bindeman, I.N. and Barth, A.P., 2011. Zircon from historic eruptions in Iceland: reconstructing storage and evolution of silicic magmas. *Mineralogy and Petrology*, *102*, pp.135-161.

Cogliati, S., Sherlock, S.C., Halton, A.M., Ebinghaus, A., Kelley, S.P., Jolley, D.W. and Barry, T.L., 2021. Expanding the toolbox for dating basaltic lava sequences: ^{40}Ar–^{39}Ar dating of silicic volcanic glass from interbeds. *Journal of the Geological Society*, *178*(1), pp.jgs2019-207.

Coombs, M.L., Sisson, T.W. and Lipman, P.W., 2006. Growth history of Kilauea inferred from volatile concentrations in submarine-collected basalts. *Journal of Volcanology and Geothermal Research*, *151*(1-3), pp.19-49.

De Hoog, J.C.M., Koetsier, G.W., Bronto, S., Sriwana, T. and Van Bergen, M.J., 2001. Sulfur and chlorine degassing from primitive arc magmas: temporal changes during the 1982–1983 eruptions of Galunggung (West Java, Indonesia). *Journal of Volcanology and Geothermal Research*, *108*(1-4), pp.55-83.

De Hoog, J.C., Taylor, B.E. and Van Bergen, M.J., 2009. Hydrogen-isotope systematics in degassing basaltic magma and application to Indonesian arc basalts. *Chemical Geology*, *266*(3-4), pp.256-266.

Denton, J.S., Tuffen, H., Gilbert, J.S. and Odling, N., 2009. The hydration and alteration of perlite and rhyolite. *Journal of the Geological Society*, *166*(5), pp.895-904.

Dixon, J.E., Stolper, E. and Delaney, J.R., 1988. Infrared spectroscopic measurements of CO2 and H2O in Juan de Fuca Ridge basaltic glasses. *Earth and Planetary Science Letters*, *90*(1), pp.87-104.

Dixon, J.E., Filiberto, J.R., Moore, J.G. and Hickson, C.J., 2002. Volatiles in basaltic glasses from a subglacial volcano in northern British Columbia (Canada): implications for ice sheet thickness and mantle volatiles. *Geological Society, London, Special Publications*, *202*(1), pp.255-271.

Dixon, J.E., Bindeman, I.N., Kingsley, R.H., Simons, K.K., Le Roux, P.J., Hajewski, T.R., Swart, P., Langmuir, C.H., Ryan, J.G., Walowski, K.J. and Wada, I., 2017. Light stable isotopic compositions of enriched mantle sources: Resolving the dehydration paradox. *Geochemistry, Geophysics, Geosystems*, *18*(11), pp.3801-3839.

Eason, D.E., Sinton, J.M., Grönvold, K. and Kurz, M.D., 2015. Effects of deglaciation on the petrology and eruptive history of the Western Volcanic Zone, Iceland. *Bulletin of Volcanology*, *77*, pp.1-27.

Eichelberger, J.C., Izbekov, P.E. and Browne, B.L., 2006. Bulk chemical trends at arc volcanoes are not liquid lines of descent. *Lithos*, *87*(1-2), pp.135-154.

Edwards, B., Magnússon, E., Thordarson, T., Guđmundsson, M.T., Höskuldsson, A., Oddsson, B. and Haklar, J., 2012. Interactions between lava and snow/ice during the 2010 Fimmvörðuháls eruption, south-central Iceland. *Journal of Geophysical Research: Solid Earth*, *117*(B4).

Flude, S., Burgess, R. and McGarvie, D.W., 2008. Silicic volcanism at Ljósufjöll, Iceland: insights into evolution and eruptive history from Ar–Ar dating. *Journal of Volcanology and Geothermal Research*, *169*(3-4), pp.154-175.

Halldórsson, S.A., Marshall, E.W., Caracciolo, A., Matthews, S., Bali, E., Rasmussen, M.B., Ranta, E., Robin, J.G., Guðfinnsson, G.H., Sigmarsson, O. and Maclennan, J., 2022. Rapid shifting of a deep magmatic source at Fagradalsfjall volcano, Iceland. *Nature*, *609*(7927), pp.529-534.

Hampton, R.L., Bindeman, I.N., Stern, R.A., Coble, M.A. and Rooyakkers, S.M., 2021. A microanalytical oxygen isotopic and U-Th geochronologic investigation and modeling of rhyolite petrogenesis at the Krafla Central Volcano, Iceland. *Journal of Volcanology and Geothermal Research*, *414*, p.107229.

Hjartardóttir, Á.R., Einarsson, P., Bramham, E. and Wright, T.J., 2012. The Krafla fissure swarm, Iceland, and its formation by rifting events. *Bulletin of Volcanology*, *74*, pp.2139-2153.

Höskuldsson, A., Sparks, R.S. and Carroll, M.R., 2006. Constraints on the dynamics of subglacial basalt eruptions from geological and geochemical observations at Kverkfjöll, NE-Iceland. *Bulletin of Volcanology*, *68*, pp.689-701.

Jakobsson, S.P. and Gudmundsson, M.T., 2008. Subglacial and intraglacial volcanic formations in Iceland. *Jökull*, *58*, pp.179-196.

Kjartansson, G. 1943. Geology of Árnessýsla. (In Icelandic). *In: Ánesingasaga I*, 104–119

Lacasse, C., Sigurdsson, H., Carey, S.N., Jóhannesson, H., Thomas, L.E. and Rogers, N.W., 2007. Bimodal volcanism at the Katla subglacial caldera, Iceland: insight into the geochemistry and petrogenesis of rhyolitic magmas. *Bulletin of Volcanology*, *69*, pp.373-399.

Lerner, G.A., Piispa, E.J., Bowles, J.A. and Ort, M.H., 2022. Paleomagnetism and rock magnetism as tools for volcanology. *Bulletin of Volcanology*, *84*(3), p.24.

Licciardi, J.M., Kurz, M.D. and Curtice, J.M., 2007. Glacial and volcanic history of Icelandic table mountains from cosmogenic ^{3}He exposure ages. *Quaternary Science Reviews*, *26*(11-12), pp.1529-1546.

MacDonald, G.A. and Katsura, T., 1964. Chemical composition of Hawaiian lavas. *Journal of petrology*, *5*(1), pp.82-133.

Magnússon, E., Gudmundsson, M.T., Roberts, M.J., Sigurðsson, G., Höskuldsson, F. and Oddsson, B., 2012. Ice-volcano interactions during the 2010 Eyjafjallajökull eruption, as revealed by airborne imaging radar. *Journal of Geophysical Research: Solid Earth*, *117*(B7).

McIntosh, I.M., Aoki, K., Yanagishima, T., Kobayashi, M., Murata, M. and Suzuki, T., 2022. Reconstruction of submarine eruption processes from FTIR volatile analysis of marine tephra: Example of Oomurodashi volcano, Japan. *Frontiers in Earth Science*, *10*, p.963392.

McIntosh, I.M., Tani, K., Nichols, A.R., Chang, Q. and Kimura, J.I., 2022. Past eruptions of a newly discovered active, shallow, silicic submarine volcano near Tokyo Bay, Japan. *Geology*, *50*(10), pp.1111-1115.

Newman, S. and Lowenstern, J.B., 2002. VolatileCalc: a silicate melt–H2O–CO2 solution model written in Visual Basic for excel. *Computers & Geosciences*, *28*(5), pp.597-604.

Nichols, A.R. and Wysoczanski, R.J., 2007. Using micro-FTIR spectroscopy to measure volatile contents in small and unexposed inclusions hosted in olivine crystals. *Chemical Geology*, *242*(3-4), pp.371-384.

Oladottir, B.A., Thordarson, T., Larsen, G. and Sigmarsson, O., 2007. Survival of the Mýrdalsjökull ice cap through the Holocene thermal maximum: evidence from sulphur contents in Katla tephra layers (Iceland) from the last∽ 8400 years. *Annals of Glaciology*, *45*, pp.183-188.

Owen, J., Tuffen, H. and McGarvie, D., 2018. Magma degassing in the effusive-explosive subglacial rhyolitic eruption at Dalakvisl, Torfajokull, Iceland: insights into quenching pressures, palaeo-ice thickness, and edifice erosion. *JÖKULL*, *68*, pp.67-94.

Pagli, C. and Sigmundsson, F., 2008. Will present day glacier retreat increase volcanic activity? Stress induced by recent glacier retreat and its effect on magmatism at the Vatnajökull ice cap, Iceland. *Geophysical Research Letters*, *35*(9).

Patton, H., Hubbard, A., Bradwell, T. and Schomacker, A., 2017. The configuration, sensitivity and rapid retreat of the Late Weichselian Icelandic ice sheet. *Earth-Science Reviews*, *166*, pp.223-245.

Pinton, A., Giordano, G., Speranza, F. and Þórðarson, Þ., 2018. Paleomagnetism of Holocene lava flows from the Reykjanes Peninsula and the Tungnaá lava sequence (Iceland): implications for flow correlation and ages. *Bulletin of Volcanology*, *80*, pp.1-19.

Russell, J.K., Edwards, B.R., Porritt, L. and Ryane, C., 2014. Tuyas: a descriptive genetic classification. *Quaternary Science Reviews*, *87*, pp.70-81.

Rutherford, M.J., 2008. Magma ascent rates. *Reviews in Mineralogy and Geochemistry*, *69*(1), pp.241-271.

Schiellerup, H., 1995. Generation and equilibration of olivine tholeiites in the northern rift zone of Iceland. A petrogenetic study of the Bláfjall Table Mountain. *Journal of volcanology and geothermal research*, *65*(3-4), pp.161-179.

Sigurbergsdóttir, A.M., 2023. *Glaciovolcanic edifices: Correlation of passage zone with ice sheet slope at Bláfjall tuya, NE Iceland*. Magister Scientairum thesis in Geology

Taylor, B.E., Eichelberger, J.C. and Westrich, H.R., 1983. Hydrogen isotopic evidence of rhyolitic magma degassing during shallow intrusion and eruption. *Nature*, *306*(5943), pp.541-545.

Thordarson, T. and Höskuldsson, Á., 2014. *Iceland*. Dunedin Academic Press Ltd.

Tuffen, H., Owen, J. and Denton, J., 2010. Magma degassing during subglacial eruptions and its use to reconstruct palaeo-ice thicknesses. *Earth-Science Reviews*, *99*(1-2), pp.1-18.

Von Aulock, F.W., Kennedy, B.M., Schipper, C.I., Castro, J.M., Martin, D.E., Oze, C., Watkins, J.M., Wallace, P.J., Puskar, L., Bégué, F. and Nichols, A.R.L., 2014. Advances in Fourier transform infrared spectroscopy of natural glasses: From sample preparation to data analysis. *Lithos*, *206*, pp.52-64.

de Vries, M.V.W., Bingham, R.G. and Hein, A.S., 2018. A new volcanic province: an inventory of subglacial volcanoes in West Antarctica.

Werner, R., Schmincke, H.U. and Sigvaldason, G., 1996. A new model for the evolution of table mountains: volcanological and petrological evidence from Herdubreid and Herdubreidartögl volcanoes (Iceland). *Geologische Rundschau*, *85*, pp.390-397.

Yokoyama, T., Okumura, S. and Nakashima, S., 2008. Hydration of rhyolitic glass during weathering as characterized by IR microspectroscopy. *Geochimica et Cosmochimica Acta*, *72*(1), pp.117-125.

Appendix A: Sample list and GPS locations

Sample Name	Rock Type	°N (Latitude)	°W (Longitude)	Elevation (m)
GS22-01	Hyaloclastite	65°47'35.10"N	16°52'27.36"W	488 m
GS22-02	Hyaloclastite	65°47'30.65"N	16°52'24.45"W	604 m
GS22-03	Hyaloclastite	65°47'25.37"N	16°52'38.04"W	625 m
GS22-04	Hyaloclastite breccia	65°47'49.39"N	16°52'18.18"W	551 m
GS22-06	Hyaloclastite breccia	65°45'56.14"N	16°50'23.15"W	560 m
GS22-07	Hyaloclastite	65°45'56.57"N	16°50'14.53"W	538 m
GS23-01	Hyaloclastite breccia	65°46'58.80"N	16°55'55.88"W	485 m
GS23-02	Hyaloclastite breccia	65°46'24.66"N	16°55'38.76"W	570 m
GS23-03	Hyaloclastite breccia	65°46'24.66"N	16°55'19.32"W	773 m
GS23-04	Hyaloclastite breccia	65°45'51.60"N	16°55'24.66"W	571 m
GS23-05	Hyaloclastite breccia	65°45'20.99"N	16°55'11.71"W	559 m
GS23-06	Hyaloclastite Breccia	65°45'22.33"N	16°55'18.82"W	576 m
GS23-07	Hyaloclastite	65°43'34.86"N	16°55'18.60"W	500 m
BF22-01	Hyaloclastite breccia	65°34'17.15"N	16°37'11.19"W	423 m
BF22-02	Hyaloclastite	65°34'15.98"N	16°37'9.53"W	433 m
BF22-03	Hyaloclastite	65°34'6.92"N	16°37'26.83"W	479 m
BF22-04	Pillow basalt	65°34'7.24"N	16°37'28.26"W	476 m
BF22-05	Hyaloclastite	65°34'0.92"N	16°37'31.76"W	514 m
BF22-06	Hyaloclastite	65°33'53.64"N	16°37'35.16"W	590 m

BF22-07	Hyaloclastite	65°33'42.46"N	16°37'46.82"W	569 m
BF22-08	Hyaloclastite	65°33'39.29"N	16°37'51.73"W	601 m
BF22-09	Hyaloclastite	65°34'53.79"N	16°35'51.63"W	449 m
BF22-10	Porphyritic Basalt	65°34'21.88"N	16°36'45.10"W	433 m
BF22-11	Hyaloclastite	65°33'23.38"N	16°36'45.91"W	459 m
BF22-12	Hyaloclastite breccia	65°32'53.27"N	16°37'24.00"W	518 m
BF22-13	Hyaloclastite	65°32'53.09"N	16°37'28.35"W	526 m
BF22-14	Hyaloclastite	65°32'53.12"N	16°37'28.35"W	551 m
BF23-01	Hyaloclastite breccia	65°33'44.00"N	16°38'26.64"W	712 m
BF23-02	Hyaloclastite breccia	65°33'47.28"N	16°38'26.64"W	556 m
BF23-03	Hyaloclastite breccia	65°32'40.14"N	16°37'31.44"W	602 m
BF23-04	Hyaloclastite breccia	65°32'40.68"N	16°37'35.58"W	583 m
BL22-01	Hyaloclastite breccia	65°28'43.82"N	16°52'54.43"W	379 m
BL22-02	Hyaloclastite breccia	65°28'42.89"N	16°52'40.56"W	394 m
BL22-03	Hyaloclastite breccia	65°28'56.93"N	16°51'34.45"W	439 m
BL22-04	Pillow basalt	65°29'20.21"N	16°51'14.86"W	410 m
BL22-05	Hyaloclastite	65°29'17.14"N	16°51'0.46"W	446 m
BL22-06	Pillow basalt	65°30'40.72"N	16°51'5.90"W	400 m
BL23-01	Hyaloclastite breccia	65°28'23.82"N	16°50'55.32"W	803 m
BL23-02	Hyaloclastite breccia	65°27'9.78"N	16°53'15.42"W	831 m
BL23-03	Hyaloclastite breccia	65°28'20.10"N	16°53'32.40"W	466 m

BL23-04	Hyaloclastite breccia	65°27'4.14"N	16°49'40.26"W	824 m
BL23-05	Hyaloclastite breccia	65°26'21.90"N	16°48'36.06"W	783 m
BL23-06	Hyaloclastite breccia	65°25'25.02"N	16°48'51.72"W	725 m
BL23-07	Hyaloclastite breccia	65°24'50.82"N	16°50'55.56"W	934 m
HE23-01	Hyaloclastite breccia	65° 9'22.86"N	16°20'44.88"W	650 m
HE23-02	Hyaloclastite	65°10'51.42"N	16°23'31.50"W	740 m
HE23-03	Hyaloclastite breccia	65°10'51.92"N	16°23'11.47"W	860 m
HE23-04	Hyaloclastite breccia	65°10'51.46"N	16°23'4.27"W	911 m
HE23-05	Pillow basalt	65°10'48.36"N	16°22'48.00"W	1,013 m
HE23-06	Hyaloclastite breccia	65°10'47.68"N	16°22'26.65"W	1,132 m
HE23-07	Hyaloclastite breccia	65°10'44.08"N	16°22'10.52"W	1,272 m
HE23-08	Crater rim tachylite	65°10'25.68"N	16°20'52.91"W	1,642 m

Appendix B: Electron microprobe data

TOTAL	97.30	99.32	96.50	97.11	99.09	99.42	98.00	98.45	99.73
SO_3 ppm	864.73	382.18	368.97	706.02	753.46	549.97	1646.52	1693.75	1864.88
TiO_2/FeO	0.21	0.21	0.20	0.21	0.21	0.21	0.13	0.14	0.13
MgO	6.96	7.04	7.05	7.06	7.07	7.19	7.26	7.32	7.32
TiO_2	2.37	2.36	2.32	2.35	2.34	2.37	1.54	1.58	1.56
P_2O_5	0.19	0.27	0.23	0.29	0.25	0.30	0.18	0.22	0.21
K_2O	0.22	0.21	0.26	0.22	0.23	0.22	0.30	0.26	0.24
SO_3	0.09	0.04	0.04	0.07	0.08	0.05	0.16	0.17	0.19
MnO	0.32	0.14	0.18	0.22	0.25	0.14	0.04	0.18	0.24
FeO	11.14	11.35	11.39	11.40	11.41	11.43	11.58	11.67	11.81
CaO	11.42	11.49	11.52	11.58	11.68	11.70	11.98	12.05	12.06
Al_2O_3	13.91	13.98	13.51	13.48	14.06	13.87	14.63	15.04	14.89
SiO_2	46.99	47.15	47.45	48.11	48.12	48.17	48.18	48.24	48.32
Na_2O	2.07	2.39	2.02	2.06	2.03	2.38	2.07	2.26	2.07
	GS22-06AR	**GS22_06AR**	**GS22_04A**	**GS22_04A**	**GS22_07A**	**GS22_07A**	**GS22-04A**	**GS22-04A**	**GS22-04A**

97.82	99.27	99.04	98.73	99.27	99.32	99.00	98.54	100.36	99.48	99.22
1444.83	1606.31	1272.42	559.98	438.93	186.04	199.07	491.42	495.62	365.55	360.88
0.15	0.14	0.14	0.18	0.20	0.20	0.20	0.19	0.19	0.19	0.20
7.36	7.37	7.38	7.39	7.39	7.39	7.41	7.48	7.57	7.58	7.63
1.74	1.71	1.74	2.14	2.40	2.39	2.38	2.31	2.39	2.36	2.49
0.21	0.21	0.17	0.22	0.26	0.28	0.27	0.27	0.27	0.28	0.27
0.31	0.25	0.28	0.20	0.21	0.23	0.20	0.21	0.21	0.20	0.20
0.14	0.16	0.13	0.06	0.04	0.02	0.02	0.05	0.05	0.04	0.04
0.21	0.17	0.20	0.23	0.21	0.26	0.19	0.17	0.20	0.22	0.23
11.90	11.97	11.99	12.03	12.05	12.09	12.16	12.16	12.40	12.42	12.44
12.15	12.22	12.23	12.24	12.27	12.30	12.31	12.31	12.33	12.40	12.41
14.30	14.49	14.35	14.18	13.73	13.79	13.90	13.66	13.61	13.49	13.57
48.34	48.35	48.45	48.46	48.53	48.59	48.75	48.79	49.07	49.07	49.19
2.24	2.30	2.29	2.24	1.83	2.16	2.15	2.14	2.14	1.98	2.09
GS22-06A	**GS22-06A**	**GS22-06A**	**GS22-07A**	**GS22_01 B**	**GS22_01 B**	**GS22_02 B**	**GS22_02 B**	**GS22_03 B**	**GS22_03 B**	**GS22_04 B**

99.16	98.96	100.21	100.65	100.32	99.07	100.10	99.81	100.80	100.57	100.26
281.42	437.48	390.17	437.02	93.73	234.66	390.81	124.96	187.48	-15.70	437.09
0.18	0.19	0.18	0.18	0.19	0.18	0.18	0.19	0.18	0.19	0.17
7.68	7.56	7.57	7.43	7.55	7.56	7.55	7.64	7.41	7.49	7.47
2.40	2.18	2.24	2.22	2.27	2.06	2.19	2.24	2.20	2.26	2.14
0.23	0.27	0.20	0.21	0.24	0.16	0.33	0.22	0.22	0.22	0.25
0.23	0.18	0.18	0.20	0.20	0.21	0.21	0.21	0.20	0.19	0.18
0.03	0.04	0.04	0.04	0.01	0.02	0.04	0.01	0.02	0.00	0.04
0.17	0.17	0.24	0.22	0.22	0.24	0.19	0.19	0.22	0.19	0.11
13.35	11.77	12.13	12.18	11.78	11.52	12.14	12.04	12.18	12.01	12.35
12.41	11.93	12.31	12.52	12.10	11.91	12.05	12.11	12.21	12.50	12.23
13.64	14.05	14.19	14.32	14.44	14.46	14.16	14.38	14.12	13.96	14.23
49.33	48.63	49.05	49.43	49.37	48.73	49.23	48.56	49.70	49.43	49.00
2.28	2.06	2.02	1.83	2.04	2.08	1.95	2.16	2.25	2.21	2.17
GS22_04 B	**GS2302_ a**	**GS2302_ b**	**GS2302_c**	**GS2302_ d**	**GS2303_ a**	**GS2303_ b**	**GS2303_c**	**GS2303_ d**	**GS2304_ a**	**GS2304_ b**

101.19	100.13	100.67	99.10	100.38	100.85	99.59	98.74	99.56	100.12	93.85
202.72	530.14	531.48	655.81	358.71	623.53	31.24	593.26	62.41	250.08	768.68
0.18	0.19	0.20	0.21	0.19	0.18	0.19	0.20	0.19	0.19	0.25
7.59	7.30	7.23	7.30	7.13	7.25	7.52	7.36	7.36	7.46	6.06
2.29	2.30	2.41	2.42	2.32	2.39	2.19	2.26	2.25	2.23	2.81
0.28	0.26	0.29	0.24	0.19	0.20	0.23	0.20	0.19	0.21	0.22
0.19	0.19	0.17	0.23	0.22	0.21	0.21	0.16	0.19	0.20	0.38
0.02	0.05	0.05	0.07	0.04	0.06	0.00	0.06	0.01	0.03	0.08
0.27	0.24	0.20	0.24	0.19	0.22	0.26	0.21	0.21	0.20	0.22
12.69	12.07	12.08	11.70	12.19	13.06	11.68	11.41	11.81	11.84	11.44
12.38	12.39	12.28	12.17	12.55	12.65	12.35	12.27	12.15	12.09	10.81
14.20	14.27	13.69	13.70	13.93	13.95	14.11	13.89	13.97	14.09	12.79
49.04	48.52	50.08	48.90	49.31	48.56	48.72	48.90	49.19	49.30	46.74
2.17	2.48	2.15	2.15	2.22	2.25	2.26	1.98	2.11	2.34	2.25
GS2304_c	**GS2304_d**	**GS2305_a**	**GS2305_b**	**GS2305_c**	**GS2305_d**	**GS2306_a**	**GS2306_b**	**GS2306_c**	**GS2306_d**	**GS2301_a test**

99.20	97.25	97.23	98.23	97.41	99.24	98.52	98.78	100.36	99.63	97.74
127.32	156.78	266.86	109.73	518.25	627.81	408.19	235.42	502.23	1238.28	977.35
0.12	0.24	0.23	0.22	0.23	0.20	0.21	0.20	0.20	0.17	0.16
0.19	5.98	6.03	6.11	6.08	6.83	6.82	6.90	6.77	4.11	4.15
0.15	2.93	2.84	2.81	2.82	2.44	2.49	2.42	2.49	1.60	1.58
-0.01	0.23	0.23	0.25	0.26	0.21	0.20	0.23	0.28	0.17	0.15
0.05	0.35	0.41	0.42	0.41	0.23	0.20	0.25	0.22	0.35	0.27
0.01	0.02	0.03	0.01	0.05	0.06	0.04	0.02	0.05	0.12	0.10
-0.03	0.20	0.19	0.14	0.19	0.19	0.20	0.18	0.22	0.14	0.20
1.28	12.32	12.54	13.01	12.44	12.22	11.81	12.40	12.64	9.40	9.88
13.94	11.72	11.44	11.43	11.33	12.52	12.54	12.36	12.74	8.90	8.91
30.03	12.92	12.74	12.82	12.80	13.48	13.38	13.30	13.58	15.05	14.95
50.55	47.87	48.10	48.59	48.39	48.80	48.67	48.49	49.14	47.99	48.01
3.07	2.64	2.58	2.59	2.64	2.15	2.15	2.03	2.06	2.05	1.93
GS2301_ a test fsp	**GS2301_ a**	**GS2301_ b**	**GS2301_c**	**GS2301_ d**	**GS2203B _a**	**GS2203B _b**	**GS2203B _c**	**GS2203B _d**	**BF22-02BR**	**BF22-02BR**

99.46	97.54	99.86	100.91	98.98	100.25	98.90	99.07	100.51	98.79	100.01
1836.71	1582.95	1335.56	1053.86	1481.28	1509.45	1594.21	1361.93	1100.21	1646.96	1615.37
0.16	0.17	0.17	0.17	0.15	0.15	0.15	0.15	0.16	0.07	0.07
4.36	4.50	4.51	4.52	4.53	4.58	4.62	4.63	6.90	6.96	6.99
1.64	1.74	1.73	1.73	1.60	1.61	1.62	1.64	1.70	0.79	0.77
0.17	0.18	0.18	0.18	0.15	0.20	0.16	0.19	0.17	0.07	0.08
0.26	0.31	0.28	0.29	0.28	0.30	0.25	0.27	0.28	0.08	0.05
0.18	0.16	0.13	0.11	0.15	0.15	0.16	0.14	0.11	0.16	0.16
0.29	0.12	0.11	0.27	0.23	0.23	0.26	0.19	0.20	0.12	0.06
9.99	10.16	10.17	10.41	10.45	10.53	10.61	10.65	10.68	10.70	10.74
9.03	9.09	9.18	9.25	9.30	9.31	9.37	9.44	11.37	11.39	11.39
15.06	14.54	14.55	14.56	15.02	15.22	14.96	14.65	14.90	15.01	14.99
48.28	48.34	48.42	48.45	48.59	48.60	48.64	48.65	48.68	48.72	48.73
2.26	2.01	2.52	2.31	2.38	2.35	2.38	2.34	2.13	1.52	1.85
BF22-02BR	**BF22-07BR**	**BF22-07BR**	**BF22-07BR**	**BF22-01BR**	**BF22-01BR**	**BF22-01BR**	**BF22-06BR**	**BF22-06BR**	**BF22-09BR**	**BF22-09BR**

97.86	98.39	100.99	97.88	99.11	99.39	99.05	98.09	98.22	100.04	100.85
1150.55	1595.66	698.05	695.94	184.13	2062.56	1417.86	1475.51	1298.78	2791.13	3001.79
0.16	0.16	0.16	0.16	0.16	0.15	0.15	0.15	0.15	0.27	0.27
6.99	7.01	7.05	7.06	7.11	7.13	7.14	7.16	7.20	7.20	7.23
1.73	1.70	1.72	1.76	1.74	1.62	1.67	1.67	1.66	3.06	3.01
0.21	0.17	0.24	0.22	0.19	0.17	0.19	0.20	0.17	0.31	0.41
0.27	0.29	0.29	0.32	0.27	0.28	0.26	0.27	0.27	0.79	0.85
0.12	0.16	0.07	0.07	0.02	0.21	0.14	0.15	0.13	0.28	0.30
0.26	0.18	0.35	0.24	0.28	0.11	0.22	0.14	0.17	0.26	0.31
10.77	10.78	10.88	10.93	10.94	11.00	11.03	11.16	11.16	11.18	11.22
11.46	11.47	11.47	11.49	11.49	11.51	11.51	11.51	11.51	11.52	11.53
14.32	14.26	14.78	14.49	14.58	14.91	15.12	14.80	14.81	13.00	12.01
48.73	48.73	48.88	48.94	48.95	49.00	49.02	49.07	49.08	49.08	49.11
2.16	2.26	2.36	1.92	2.39	2.20	2.63	2.02	2.04	2.72	2.98
BF22_05BR	**BF22_05BR**	**BF22_08B**	**BF22_08B**	**BF22_08B**	**BF22_04B**	**BF22_04B**	**BF22-03B**	**BF22-03B**	**BF22_10B**	**BF22_10B**

98.93	100.32	100.91	101.50	99.00	100.23	98.64	100.58	98.66	97.62	99.52
163.31	483.45	290.51	368.56	2356.07	2275.09	2372.26	2302.56	2134.69	1661.97	1594.22
0.15	0.15	0.16	0.15	0.26	0.26	0.26	0.26	0.14	0.14	0.14
7.24	7.24	7.29	7.32	7.39	7.40	7.41	7.42	7.48	7.49	7.50
1.66	1.67	1.75	1.69	3.01	2.96	2.94	2.99	1.57	1.64	1.64
0.18	0.21	0.20	0.22	0.36	0.42	0.37	0.34	0.12	0.16	0.19
0.31	0.35	0.28	0.22	0.62	0.71	0.67	0.70	0.31	0.28	0.26
0.02	0.05	0.03	0.04	0.24	0.23	0.24	0.23	0.21	0.17	0.16
0.13	0.16	0.25	0.14	0.23	0.26	0.20	0.27	0.27	0.13	0.19
11.23	11.26	11.28	11.34	11.38	11.47	11.52	11.58	11.60	11.76	11.77
11.53	11.56	11.57	11.58	11.58	11.59	11.60	11.61	11.61	11.61	11.62
15.05	15.02	15.77	15.42	13.20	12.79	12.46	12.78	14.83	14.73	14.72
49.13	49.15	49.15	49.17	49.18	49.20	49.22	49.22	49.23	49.29	49.31
2.17	2.43	2.08	2.06	2.67	2.72	2.40	2.67	2.16	2.12	2.32
BF22_11B	**BF22_11B**	**BF22_12B**	**BF22_12B**	**BF22_13B**	**BF22_13B**	**BF22_14B**	**BF22_14B**	**BF22-01A**	**BF22-01A**	**BF22-02A**

98.90	98.29	99.42	98.34	99.68	97.72	99.17	98.44	98.34	99.40	98.66
1502.12	1433.19	1529.81	1727.35	1487.32	1291.45	1187.72	1354.58	1417.57	1188.56	1592.53
0.13	0.13	0.14	0.13	0.13	0.14	0.14	0.13	0.13	0.14	0.14
7.54	7.55	7.57	7.59	7.59	7.61	7.62	7.63	7.63	7.66	7.68
1.58	1.57	1.66	1.58	1.60	1.66	1.66	1.55	1.64	1.75	1.75
0.15	0.12	0.19	0.18	0.18	0.16	0.20	0.19	0.16	0.17	0.17
0.29	0.37	0.32	0.27	0.27	0.35	0.35	0.36	0.56	0.29	0.29
0.15	0.14	0.15	0.17	0.15	0.13	0.12	0.14	0.14	0.12	0.16
0.09	0.18	0.14	0.12	0.17	0.25	0.21	0.06	0.08	0.19	0.28
11.87	11.91	11.95	11.97	12.09	12.11	12.19	12.21	12.25	12.34	12.37
11.63	11.66	11.66	11.67	11.67	11.68	11.70	11.72	11.72	11.73	11.75
14.85	14.62	14.53	14.86	14.89	14.13	14.09	14.36	14.07	14.40	14.18
49.32	49.35	49.47	49.53	49.57	49.61	49.65	49.68	49.70	49.73	49.76
2.22	2.18	2.37	2.03	2.13	2.10	2.19	2.52	2.52	2.11	2.09
BF22-02A	**BF22-03A**	**BF22-03A**	**BF22-04A**	**BF22-04A**	**BF22-05A**	**BF22-05A**	**BF22-06A**	**BF22-06A**	**BF22-07A**	**BF22-07A**

98.76	97.86	100.03	99.52	98.18	97.84	98.89	97.21	98.43	99.18	99.76
907.66	473.70	1623.56	2013.36	2724.23	2338.89		101.52	321.33	822.89	2074.87
0.14	0.14	0.05	0.06	0.20	0.19	0.11	0.10	0.11	0.10	0.19
7.69	7.69	7.72	7.94	7.94	7.94	7.97	7.97	8.77	8.78	8.88
1.71	1.72	0.78	0.85	3.02	3.02	1.74	1.64	1.78	1.64	3.08
0.16	0.17	0.06	0.03	0.39	0.40	0.24	0.26	0.22	0.16	0.36
0.40	0.37	0.05	0.04	0.67	0.64	0.30	0.32	0.34	0.34	0.72
0.09	0.05	0.16	0.20	0.27	0.23	0.00	0.01	0.03	0.08	0.21
0.29	0.09	0.32	0.25	0.29	0.21	0.11	0.28	0.23	0.17	0.31
12.38	12.66	14.27	14.89	15.32	15.83	16.01	16.02	16.05	16.09	16.29
11.76	11.78	11.78	11.81	11.94	11.97	12.07	12.09	13.76	13.83	13.85
14.29	14.45	15.11	14.97	12.41	12.69	15.00	14.78	14.78	15.00	12.50
49.78	49.79	49.79	49.83	49.85	49.94	49.98	50.02	50.07	50.20	50.40
2.31	2.21	1.68	1.56	2.67	3.02	2.02	1.95	2.07	1.91	2.74
BF22-08A	**BF22-08A**	**BF22-09A**	**BF22-09A**	**BF22-10A**	**BF22-10A**	**BF22-11A**	**BF22-11A**	**BF22_12 A**	**BF22_12 A**	**BF22_13 A**

98.00	99.36	97.48	96.83	98.59	97.28	98.48	97.09	97.12	98.76	98.08
2201.00	456.22	676.71	487.92	220.36	943.81	1007.14	960.15	897.95	1906.02	1513.33
0.18	0.15	0.16	0.17	0.16	0.15	0.14	0.14	0.15	0.14	0.15
9.00	7.07	7.05	7.14	6.98	7.75	7.79	7.63	7.53	7.46	7.13
3.01	1.83	1.80	1.90	1.80	1.60	1.54	1.49	1.52	1.59	1.65
0.34	0.20	0.16	0.17	0.24	0.10	0.12	0.04	0.16	0.15	0.16
0.68	0.34	0.31	0.31	0.28	0.14	0.19	0.19	0.16	0.29	0.25
0.22	0.05	0.07	0.05	0.02	0.09	0.10	0.10	0.09	0.19	0.15
0.29	0.20	0.16	0.19	0.18	0.18	0.18	0.20	0.22	0.16	0.19
16.48	12.24	11.32	10.87	11.05	10.41	10.78	10.38	10.45	11.11	11.30
13.88	11.67	11.86	11.79	11.90	12.49	12.75	12.60	12.59	11.87	11.34
12.56	13.88	14.00	14.09	14.13	14.32	14.42	14.44	14.17	14.68	14.63
51.22	49.49	48.55	48.33	49.60	48.16	48.42	48.01	48.13	48.96	48.98
2.50	2.29	2.17	1.94	2.33	1.89	2.03	1.95	2.02	2.20	2.30
BF22_13 A	**BF2303_a**	**BF2303_b**	**BF2303_c**	**BF2303_d**	**BF2302_a**	**BF2302_b**	**BF2302_c**	**BF2302_d**	**BF2202A _a**	**BF2202A _b**

96.44	97.21	97.24	97.01	97.77	96.84	99.19	98.95	98.48	98.18	100.88
1764.92	1606.35	866.35	31.52	330.55	489.00	551.60	598.29	173.39	110.37	-110.00
0.15	0.15	0.15	0.17	0.16	0.16	0.16	0.16	0.16	0.16	0.08
7.39	7.23	7.51	7.50	7.61	7.54	7.43	7.31	7.22	7.34	15.06
1.63	1.68	1.60	1.76	1.78	1.68	1.73	1.83	1.80	1.72	0.80
0.23	0.23	0.26	0.16	0.22	0.29	0.22	0.10	0.20	0.26	-0.05
0.25	0.26	0.32	0.32	0.32	0.32	0.36	0.34	0.32	0.34	-0.01
0.18	0.16	0.09	0.00	0.03	0.05	0.06	0.06	0.02	0.01	-0.01
0.20	0.24	0.20	0.16	0.20	0.17	0.15	0.22	0.18	0.24	0.27
11.08	11.23	11.04	10.64	11.30	10.45	11.04	11.27	11.23	10.96	9.98
11.42	11.43	11.44	12.01	11.59	11.47	11.74	11.62	11.56	11.39	19.55
14.54	14.61	14.65	14.44	14.62	14.48	14.70	14.63	14.61	14.54	2.66
47.35	47.81	47.73	47.77	47.91	48.24	49.38	49.30	49.07	49.09	52.21
2.12	2.25	2.32	2.17	2.14	2.09	2.30	2.27	2.17	2.30	0.26
BF2202A _c	**BF2202A _d**	**BF22011 A_a**	**BF22011 A_b**	**BF22011 A_c**	**BF22011 A_d**	**BF22012 A_a**	**BF22012 A_b**	**BF22012 A_c**	**BF22012 A_d**	**BF22013B _a**

97.36	100.35	101.54	98.52	98.41	97.49	97.77	97.86	97.91	98.39	97.75
2023.67	-78.80	95.53	2433.25	2575.21	2385.37	2640.01	382.13	328.18	1732.20	1910.43
0.20	0.07	0.11	0.20	0.20	0.21	0.22	0.21	0.20	0.17	0.17
4.34	16.22	0.14	4.34	4.24	4.40	4.34	7.15	7.30	7.32	7.45
3.02	0.65	0.08	3.12	3.03	3.16	3.19	2.07	2.01	1.71	1.72
0.37	-0.01	-0.05	0.38	0.36	0.35	0.31	0.24	0.23	0.18	0.18
0.63	0.00	0.10	0.61	0.64	0.65	0.57	0.23	0.25	0.39	0.47
0.20	-0.01	0.01	0.24	0.26	0.24	0.26	0.04	0.03	0.17	0.19
0.28	0.21	0.07	0.23	0.24	0.23	0.27	0.25	0.29	0.33	0.06
15.07	9.05	0.74	15.47	14.90	14.94	14.78	9.77	10.16	10.19	10.31
9.31	18.44	14.71	9.50	9.26	9.17	8.92	11.19	11.27	11.66	11.76
12.60	2.18	30.06	12.38	12.28	12.37	12.23	14.18	13.89	15.26	14.89
48.76	53.25	52.10	49.65	50.16	49.27	49.69	47.30	47.65	47.77	47.97
2.71	0.20	3.54	2.57	2.95	2.67	3.10	2.04	1.76	2.06	2.20
BF22013B_b	**BF22013B_c**	**BF22013B_d**	**BF22014B_a**	**BF22014B_b**	**BF22014B_c**	**BF22014B_d**	**BL22_02AR**	**BL22_02AR**	**BL22_06A**	**BL22_06A**

100.42	100.16	99.36	100.21	97.79	100.91	99.66	100.52	101.90	100.41	99.82
261.78	244.06	1403.14	1919.62	144.56	248.82	130.39	459.78	344.64	699.39	379.65
0.20	0.20	0.07	0.07	0.18	0.18	0.18	0.18	0.17	0.18	0.18
7.53	7.55	7.57	7.61	7.62	7.64	7.65	7.81	7.90	7.90	7.96
2.11	2.16	0.76	0.76	2.05	2.09	2.11	2.06	2.03	2.15	2.16
0.33	0.29	0.08	0.01	0.24	0.26	0.28	0.23	0.33	0.22	0.21
0.23	0.22	0.06	0.06	0.20	0.25	0.26	0.22	0.21	0.17	0.21
0.03	0.02	0.14	0.19	0.01	0.02	0.01	0.05	0.03	0.07	0.04
0.23	0.26	0.13	0.10	0.18	0.20	0.23	0.29	0.30	0.23	0.20
10.38	10.57	10.69	11.13	11.66	11.68	11.71	11.73	11.76	11.76	11.97
11.81	11.81	12.05	12.07	12.11	12.12	12.15	12.25	12.29	12.31	12.35
14.28	14.27	15.20	15.20	14.04	14.68	14.81	14.49	14.52	14.42	14.30
48.21	48.22	48.27	48.31	48.39	48.44	48.46	48.69	48.78	49.16	49.19
2.08	2.37	1.93	1.88	2.15	2.32	1.99	2.05	2.12	2.14	2.14
BL22_01A	**BL22_01A**	**BL22_04A**	**BL22_04A**	**BL22-03AR**	**BL22_01B**	**BL22_01B**	**BL22_02B**	**BL22_02B**	**BL22_03B**	**BL22_03B**

102.63	99.94	101.33	101.71	99.93	99.30	100.80	100.85	100.84	100.49	100.25
1975.63	2012.35	2356.28	2202.21	1311.78	1850.31	124.82	15.58	202.50	499.34	234.02
0.06	0.06	0.21	0.20	0.12	0.12	0.18	0.19	0.19	0.19	0.21
8.00	8.14	8.56	8.75	8.88	9.06	7.07	6.99	7.00	6.81	7.42
0.79	0.78	2.62	2.59	1.68	1.74	2.28	2.44	2.42	2.39	2.40
0.05	0.05	0.30	0.28	0.17	0.22	0.33	0.38	0.30	0.23	0.25
0.04	0.04	0.21	0.21	0.45	0.42	0.23	0.29	0.27	0.23	0.20
0.20	0.20	0.24	0.22	0.13	0.19	0.01	0.00	0.02	0.05	0.02
0.19	0.26	0.32	0.11	0.24	0.23	0.19	0.25	0.22	0.24	0.17
12.40	12.45	12.64	12.88	14.32	15.06	12.82	12.88	12.56	12.44	11.69
12.35	12.46	12.93	13.09	13.10	13.14	12.12	12.44	12.63	12.37	12.60
15.72	15.45	14.46	14.43	15.39	15.30	13.59	13.36	13.53	13.67	13.91
49.26	49.39	49.50	49.83	50.02	50.39	49.67	49.49	49.45	49.71	49.34
2.03	1.48	2.09	2.64	2.29	2.37	2.36	2.29	2.35	2.23	2.22
BL22_04B	**BL22_04B**	**BL22_05B**	**BL22_05B**	**BL22_06B**	**BL22_06B**	**BL2301_a**	**BL2301_b**	**BL2301_c**	**BL2301_d**	**BL2302_a**

100.60	99.80	100.58	100.35	100.83	100.45	101.29	99.41	101.62	100.22	100.22
140.37	156.08	390.19	15.63	-47.00	468.36	561.87	639.96	312.05	531.29	265.52
0.18	0.18	0.19	0.18	0.17	0.18	0.17	0.17	0.17	0.17	0.18
7.35	7.25	7.41	7.49	7.61	7.52	7.54	7.66	7.74	7.71	7.61
2.19	2.20	2.22	2.14	2.04	2.15	2.10	2.04	2.13	2.05	2.10
0.36	0.32	0.31	0.42	0.32	0.24	0.24	0.28	0.25	0.23	0.28
0.24	0.21	0.19	0.22	0.24	0.28	0.20	0.23	0.21	0.20	0.21
0.01	0.02	0.04	0.00	0.00	0.05	0.06	0.06	0.03	0.05	0.03
0.24	0.15	0.18	0.12	0.21	0.18	0.17	0.19	0.18	0.24	0.17
12.14	12.49	11.75	11.58	12.03	11.79	12.01	11.86	12.36	12.15	11.61
12.58	12.07	12.35	12.34	12.22	12.28	12.54	11.96	12.43	11.79	12.20
14.12	14.03	13.96	14.35	14.26	14.21	14.35	14.49	14.77	14.70	14.59
48.99	48.72	49.89	49.48	49.68	49.39	50.14	48.48	49.20	48.80	49.20
2.29	2.33	2.29	2.11	2.18	2.24	1.96	2.14	2.28	2.30	2.18
BL2302_b	**BL2302_c**	**BL2302_d**	**BL2303_a**	**BL2303_b**	**BL2303_c**	**BL2303_d**	**BL2304_a**	**BL2304_b**	**BL2304_c**	**BL2304_d**

99.60	101.04	100.22	99.59	99.08	99.87	98.82	100.47	101.40	99.36	100.89
187.48	296.49	297.04	344.03	750.49	671.71	515.34	781.37	328.29	62.49	468.11
0.17	0.17	0.16	0.18	0.16	0.17	0.16	0.15	0.16	0.18	0.18
7.58	7.67	7.64	7.60	6.94	6.95	7.12	7.01	7.80	7.87	7.57
1.89	1.90	1.72	1.87	1.95	1.88	1.85	1.76	1.97	2.07	2.12
0.26	0.25	0.23	0.23	0.17	0.24	0.14	0.24	0.24	0.28	0.27
0.19	0.22	0.20	0.21	0.29	0.29	0.28	0.34	0.18	0.19	0.21
0.02	0.03	0.03	0.03	0.08	0.07	0.05	0.08	0.03	0.01	0.05
0.19	0.16	0.18	0.26	0.23	0.25	0.21	0.21	0.21	0.20	0.23
11.08	11.30	10.69	10.51	11.87	11.36	11.53	12.09	12.28	11.83	12.09
12.60	13.21	13.35	12.96	11.87	12.56	12.51	12.15	11.84	11.43	12.08
13.84	14.12	14.14	13.85	14.01	13.95	13.65	14.47	14.64	14.43	14.69
49.75	49.90	50.02	49.91	49.52	49.95	49.45	50.03	49.77	48.86	49.22
2.15	2.16	1.91	2.02	2.17	2.24	1.97	2.08	2.33	2.10	2.19
BL2305_a	**BL2305_b**	**BL2305_c**	**BL2305_d**	**BL2306_a**	**BL2306_b**	**BL2306_c**	**BL2306_d**	**BL2307_a**	**BL2307_b**	**BL2307_c**

102.43	96.54	97.95	97.90	97.26	97.69	98.11	97.23	98.71	98.91	97.72
593.95	691.26	517.52	-63.00	0.00	78.44	1402.23	1209.16	1589.16	1667.35	-189.20
0.17	0.16	0.24	0.24	0.25	0.25	0.15	0.14	0.15	0.15	0.20
7.60	7.05	5.73	5.78	5.65	5.82	7.43	7.34	7.46	7.51	7.09
2.13	1.79	3.10	3.14	3.04	3.08	1.56	1.55	1.53	1.59	2.33
0.22	0.21	0.28	0.33	0.27	0.35	0.18	0.11	0.15	0.16	0.29
0.18	0.22	0.47	0.43	0.52	0.47	0.20	0.21	0.20	0.20	0.20
0.06	0.07	0.05	-0.01	0.00	0.01	0.14	0.12	0.16	0.17	-0.02
0.22	0.23	0.23	0.22	0.26	0.24	0.21	0.17	0.18	0.24	0.25
12.38	11.43	13.10	12.83	12.36	12.51	10.64	10.93	10.50	10.66	11.49
11.95	11.60	11.42	10.81	11.65	11.49	12.28	13.06	12.76	12.72	12.45
14.66	13.57	12.42	12.82	12.58	12.64	14.04	13.93	14.29	14.08	13.63
50.77	47.92	48.48	48.72	48.24	48.51	49.54	47.72	49.40	49.44	47.90
2.15	1.81	1.89	1.89	1.90	1.94	1.97	2.02	2.02	2.05	2.05
BL2307_d	**HE2304_a test**	**HE2308_a**	**HE2308_b**	**HE2308_c**	**HE2308_d**	**HE2307_a**	**HE2307_b**	**HE2307_c**	**HE2307_d**	**HE2305_a**

97.77	97.46	96.67	97.70	97.38	98.97	96.84	98.27	98.03	97.94	98.58
501.89	282.49	-31.50	62.82	313.99	266.77	-189.10	1715.93	1461.70	1243.60	2280.75
0.20	0.21	0.21	0.23	0.21	0.21	0.23	0.14	0.14	0.14	0.14
7.19	7.27	7.15	6.41	6.42	6.51	6.35	7.62	7.34	7.66	7.56
2.34	2.36	2.26	2.70	2.59	2.64	2.59	1.51	1.50	1.44	1.48
0.20	0.29	0.25	0.17	0.12	0.25	0.23	0.14	0.13	0.20	0.09
0.23	0.19	0.24	0.40	0.34	0.34	0.34	0.19	0.17	0.19	0.17
0.05	0.03	0.00	0.01	0.03	0.03	-0.02	0.17	0.15	0.12	0.23
0.15	0.22	0.17	0.22	0.20	0.12	0.24	0.19	0.13	0.19	0.17
11.67	11.42	10.82	11.99	12.22	12.42	11.49	10.65	11.04	10.53	10.64
12.45	12.32	12.30	11.41	11.67	11.75	11.82	12.62	12.65	12.72	12.59
13.93	13.69	13.78	13.37	13.32	13.16	12.94	14.50	14.25	14.32	14.55
47.46	47.72	47.62	48.42	47.96	49.10	48.65	48.80	48.54	48.35	48.83
2.06	2.07	2.09	2.13	2.15	2.17	2.17	2.24	2.24	2.26	2.32
HE2305_b	**HE2305_c**	**HE2305_d**	**HE2306_a**	**HE2306_b**	**HE2306_c**	**HE2306_d**	**HE2303_a**	**HE2303_b**	**HE2303_c**	**HE2303_d**

97.89	97.71	98.70	98.39	98.33	99.61	97.40	97.66	97.67	97.74	97.41
409.35	739.90	314.83	283.33	723.99	944.41	566.74	472.42	-220.50	94.21	-110.20
0.15	0.16	0.16	0.15	0.15	0.15	0.15	0.15	0.21	0.23	0.22
6.95	6.89	6.92	6.89	7.65	7.53	7.43	7.54	6.53	6.45	6.45
1.85	1.82	1.86	1.81	1.65	1.64	1.54	1.61	2.62	2.72	2.57
0.28	0.17	0.26	0.17	0.20	0.14	0.09	0.11	0.31	0.21	0.23
0.25	0.27	0.26	0.24	0.16	0.17	0.18	0.21	0.38	0.36	0.35
0.04	0.07	0.03	0.03	0.07	0.09	0.06	0.05	-0.02	0.01	-0.01
0.17	0.18	0.22	0.17	0.12	0.14	0.17	0.18	0.16	0.21	0.16
11.96	11.33	11.95	12.06	11.04	11.18	10.38	10.90	12.22	11.89	11.92
11.45	11.65	11.79	11.68	12.63	12.45	12.39	12.54	11.34	11.70	11.73
13.88	13.80	13.88	13.95	14.44	14.50	14.31	14.30	13.22	12.96	13.00
48.62	49.18	49.42	49.14	48.14	49.62	48.62	48.36	48.38	48.66	48.45
2.33	2.41	2.42	2.47	2.47	2.48	2.54	2.55	2.56	2.60	2.64
HE2304_a	**HE2304_b**	**HE2304_c**	**HE2304_d**	**HE2302_a**	**HE2302_b**	**HE2302_c**	**HE2302_d**	**HE2301_a**	**HE2301_b**	**HE2301_c**

HE2301_d
2.76
48.58
13.06
11.99
11.82
0.20
0.03
0.38
0.40
2.79
6.44
0.24
297.96
98.16

Appendix C: FTIR data

Name	**Absorbance**	**Peak Height**	**Glass density Run 1**	**Glass density Run 2**	**Glass density Run 3**	**Initial H2O (wt. %)**	**actual H2O (wt. %)**
BF2205_A	1.203	3506.1	2806.1645	2828.9824	2829.3181	0.78	0.77
BF2205_B	1.407	3536.958	2807.9074	2826.3695	2826.7032	0.91	0.9
BF2205_C	1.16	3536.958					
BF2204_A	1.473	3536.958	2801.2091	2808.666		1.27	1.26
			2804.4292				
BF2201_A	1.406	3540.815	2872.9835	2791.2335		1.64	1.64
BF2201_B	1.407	3540.815	2800.0602	2795.5267	2794.5587	1.61	1.64
BF2201_C	1.418	3540.815					
BF2202_A	1.4	3540.815	2800.7793	2836.6445		0.39	0.39
BF2202_B	1.385	3540.815	2841.754	2837.3252		0.39	0.39
BF2202_C	1.338	3536.958					
BF2207_A	0.89	3540.815	2878.3154	2845.4552	2845.1154	0.44	0.45
BF2207_B	0.891	3536.958	2845.4552				
BF2207_C_Bad	0.92	3540.815		2845.7591		0.46	0.46
BF2209_A_Bad	0.255	3548.529	2827.1399	2871.8263		0.14	0.14
BF2209_B_Bad	0.257	3544.672	2840.3597	2885.3322		0.14	0.14

BF2209_C_Bad	0.251	3548.529					
BF2211_A_Bad	0.327	3436.673	2873.1556	2917.4973		0.16	0.16
BF2211_B_Bad	0.534	3444.387	2872.0265	2912.9715		0.26	0.26
BF2211_C_Bad	0.407	3436.673					
BF2201_Ai	0.312	3540.814	2796.7234	2833.583		0.36	0.36
BF2201_Aii	0.307	3540.814	2800.0602	2836.997	2837.338	0.36	0.35
BF2201_Aiii	0.295	3540.814					
BF2202_Ai	0.234	3540.814	2800.7793	2847.6013	2847.9462	0.07	0.06
BF2202_Aii	0.281	3540.814	2801.4892	2847.9283		0.08	0.08
BF2202_Aiii	0.454	3540.814					
BF2204_Ai	0.307	3540.814	2842.3724	2842.3724		0.26	0.26
BF2204_Aii	0.326	3540.814	2843.9166	2838.8259		0.28	0.28
BF2204_Aiii	0.395	3540.814					
BF2205_Ai	0.448	3540.814	2806.1645	2845.952		0.28	0.28
BF2205_Aii	0.36	3540.814	2807.9074	2849.402	2849.7459	0.23	0.22
BF2205_Aiii	0.409	3540.814					
BF2206_Ai	0.215	3540.814	2807.248	2846.0824		0.3	0.29
BF2206_Aii	0.222	3540.814	2809.4437	2848.0016	2848.3425	0.31	0.29

BF2206_Aiii	0.191	3540.841					
BF2212_Ai	0.225	3540.814	2896.8613	2945.0003		0.05	0.05
BF2212_Aii	0.226	3540.814	2894.6221	2942.5723		0.05	0.05
BF2212_Aiii	0.226	3540.814					
GS2201_A	0.202	3540.814	2827.4876	2877.047		0.04	0.04
GS2201_B	0.248	3540.814	2828.7555	2877.7435		0.05	0.05
GS2201_C	0.129	3544.672					
GS2202_A	0.067	3540.814	2828.7104	2878.6078		0.02	0.02
GS2202_B	0.079	3544.672	2828.5051	2878.1332		0.03	0.03
GS2202_C	0.073	3548.529					
GS2204_A	0.05	3556.243	2835.1334	2884.9643	2883.5465	0.02	0.02
GS2204_B	0.054	3560.1	2848.48	2898.3232		0.02	0.02
GS2204_C	0.057	3552.386					
GS2305_A	0.069	3540.814					
GS2305_B	0.067	3548.529	2867.1308	2864.754		0.02	0.02
GS2305_C	0.132	3540.814	2808.666	2867.1308		0.04	0.04
BF2209_A	0.223	3540.814	2763.008	2808.2024		0.12	0.12
BF2209_B	0.198	3544.672	2765.0148	2810.4866	2797.7879	0.11	0.11

BF2209_C	0.223	3544.672					
BL2201_A	0.247	3540.814	2818.9643	2866.2691		0.08	0.08
BL2201_B	0.259	3544.672	2819.0198	2866.3648		0.08	0.08
BL2201_C	0.261	3540.814					
BL2202_A	0.137	3540.814	2779.8421	2824.3172		0.18	0.18
BL2202_B	0.129	3548.529	2784.8784	2829.7908		0.17	0.17
BL2202_C	0.144	3544.672					
BL2302_A	0.134	3544.672	2874.4129	2868.48		0.04	0.04
BL2302_B	0.132	3544.672	2864.754	2874.4129		0.04	0.04
BL2302_C	0.14	3544.672					
BL2204_A	0.07	3544.672	2809.5344	2855.3947		0.09	0.09
BL2204_B	0.072	3544.672	2810.5988	2856.6976		0.09	0.09
BL2204_C	0.071	3536.957					
BL2306_A	0.047	3544.672					
BL2206_A	0.113	3540.814	2863.6903		2906.8063	0.18	0.18
BL2206_B	0.135	3544.672	2875.6042	2917.0081	2917.348	0.22	0.21
BL2206_C	0.152	3540.814					

BL2307_A	0.104	3544.672	2868.48	2867.4425		0.03	0.03
BL2307_B	0.086	3544.672					
BL2307_C	0.098	3544.672	2867.4425			0.03	0.03
GS2303_A	0.226	3540.814		2867.8905		0.06	0.06
GS2303_B	0.232	3544.672	2867.4425	2874.4376		0.06	0.06
GS2303_C	0.244	3540.814					
HE2301_A	0.325	3536.967	2874.4376	2862.4904		0.13	0.13
HE2301_B	0.331	3540.814	2862.4376	2865.1388		0.13	0.13
HE2301_C	0.331	3540.814					
HE2303_A	0.518	3540.814	2865.1388	2845.3166	2842.5235	0.22	0.22
HE2303_B	0.551	3540.814	2845.3166	2841.1238	2837.9789	0.24	0.24
HE2303_C	0.589	3540.814					
HE2304_A	0.44	3540.814	2841.1238	2839.719	2851.632	0.12	0.12
HE2304_B	0.512	3540.814	2851.632	2836.4218	2836.4218	0.14	0.14
HE2304_C	0.591	3536.957					
HE2305_A	0.126	3544.672	2851.632	2871.1986		0.04	0.04
HE2305_B	0.162	3548.529	2871.1986	2878.3154		0.05	0.05
HE2305_C	0.168	3544.672					

HE2306_A	0.144	3544.672	2912.9715	2864.6234		0.04	0.04
HE2306_B	0.154	3544.672	2864.6234	2873.2016		0.05	0.05
HE2306_C	0.156	3544.672					
HE2307_A	0.138	3536.957	2873.2016	2858.542		0.06	0.06
HE2307_B	0.145	3544.672		2834.8763		0.06	0.06
HE2307_C	0.14	3540.814					
HE2308_A	0.176	3544.672		2870.5108		0.08	0.08
HE2308_B	0.15	3544.672				0.07	0.07
HE2308_C	0.124	3560.1					

Appendix D: Ice thickness data

	Wt%H_2O	**PPMCO_2**	**Temp(°C)**	**P (bars)**	**H_2Ov mol%**	**CO2Vmol%**	**SiO_2 (wt. %)**	**Water depth (m)**	**Ice thickness (m)**
BF2207_A	0.45	0	1000	21	100.0	0.0	49	209.12	228.05
BF2207_C	0.46	0	1000	21	100.0	0.0	49	217.88	237.60
BF2207_A	0.45	10	1000	43	48.4	51.6	49	433.93	473.21555
BF2207_A	0.45	20	1000	65	32.0	68.0	49	658.67	718.29
BF2207_C	0.46	10	1000	43	49.4	50.6	49	442.70	482.77
BF2207_C	0.46	20	1000	65	32.9	67.1	49	667.43	727.85
BF2209_A_Bad	0.14	0	1000	2	100.0	0.0	49	23.88	26.05
BF2209_A_Bad	0.14	10	1000	24	9.7	90.3	49	248.63	271.14
BF2209_A_Bad	0.14	20	1000	46	5.1	94.9	49	473.29	516.13
BF2209_B_Bad	0.14	0	1000	2	100.0	0.0	49	23.88	26.05
BF2209_B_Bad	0.14	10	1000	24	9.7	90.3	49	248.63	271.14
BF2209_B_Bad	0.14	20	1000	46	5.1	94.9	49	473.29	516.13
BF2211_A	0.16	0	1000	3	100.0	0.0	49	30.60	33.37
BF2211_A	0.16	10	1000	25	12.0	88.0	49	255.32	278.43
BF2211_A	0.16	20	1000	47	6.4	93.6	49	479.98	523.43
BF2211_B	0.26	0	1000	7	100.0	0.0	49	75.39	82.21
BF2211_B	0.26	10	1000	29	25.2	74.8	49	300.10	327.26
BF2211_B	0.26	20	1000	51	14.5	85.5	49	524.67	572.16
BF2201_Ai	0.36	0	1000	14	100.0	0.0	49	138.06	150.55
BF2201_Ai	0.36	10	1000	36	38.2	61.8	49	362.79	395.63

BF2201_Ai	0.36	20	1000	58	23.7	76.3	49	587.45	640.62
BF2201_Aii	0.35	0	1000	13	100.0	0.0	49	131.01	142.86
BF2201_Aii	0.35	10	1000	35	37.0	63.0	49	355.70	387.90
BF2201_Aii	0.35	20	1000	57	22.8	77.2	49	580.36	632.89
BF2202_Aii	0.08	0	1000	1	100.0	0.0	49	8.45	9.22
BF2202_Aii	0.08	10	1000	23	3.6	96.4	49	233.26	254.37
BF2202_Aii	0.08	20	1000	45	1.9	98.1	49	457.99	499.45
BF2204_Ai	0.26	0	1000	7	100.0	0.0	49	75.39	82.21
BF2204_Ai	0.26	10	1000	29	25.2	74.8	49	300.10	327.26
BF2204_Ai	0.26	20	1000	51	14.5	85.5	49	524.67	572.16
BF2204_Aii	0.28	0	1000	8	100.0	0.0	49	86.51	94.34
BF2204_Aii	0.28	10	1000	31	27.9	72.1	49	311.17	339.33
BF2204_Aii	0.28	20	1000	53	16.3	83.7	49	535.83	584.33
BF2205_Ai	0.28	0	1000	8	100.0	0.0	49	86.51	94.34
BF2205_Ai	0.28	10	1000	31	27.9	72.1	49	311.17	339.33
BF2205_Ai	0.28	20	1000	53	16.3	83.7	49	535.83	584.33
BF2205_Aii	0.22	0	1000	5	100.0	0.0	49	55.28	60.29
BF2205_Aii	0.22	10	1000	27	19.8	80.2	49	279.94	305.28
BF2205_Aii	0.22	20	1000	49	11.1	88.9	49	504.60	550.27
BF2206_Ai	0.29	0	1000	9	100.0	0.0	49	92.35	100.71
BF2206_Ai	0.29	10	1000	31	29.3	70.7	49	317.02	345.72
BF2206_Ai	0.29	20	1000	53	17.2	82.8	49	541.64	590.67
BF2206_Aii	0.29	0	1000	9	100.0	0.0	49	92.35	100.71
BF2206_Aii	0.29	10	1000	31	29.3	70.7	49	317.02	345.72
BF2206_Aii	0.29	20	1000	53	17.2	82.8	49	541.64	590.67
BF2209_A	0.12	0	1000	2	100.0	0.0	49	17.94	19.56
BF2209_A	0.12	10	1000	24	7.4	92.6	49	242.70	264.66
BF2209_A	0.12	20	1000	46	3.9	96.1	49	467.39	509.70
BF2209_B	0.11	0	1000	1	100.0	0.0	49	15.27	16.65
BF2209_B	0.11	10	1000	24	6.4	93.6	49	240.03	261.75
BF2209_B	0.11	20	1000	46	3.3	96.7	49	464.76	506.83
BL2201_A	0.08	0	1000	1	100.0	0.0	49	8.45	9.22
BL2201_A	0.08	10	1000	23	3.6	96.4	49	233.26	254.37
BL2201_A	0.08	20	1000	45	1.9	98.1	49	457.99	499.45
BL2201_B	0.08	0	1000	1	100.0	0.0	49	8.45	9.22
BL2201_B	0.08	10	1000	23	3.6	96.4	49	233.26	254.37
BL2201_B	0.08	20	1000	45	1.9	98.1	49	457.99	499.45
BL2202_A	0.18	0	1000	4	100.0	0.0	49	38.09	41.53
BL2202_A	0.18	10	1000	26	14.6	85.4	49	262.77	286.56
BL2202_A	0.18	20	1000	48	7.9	92.1	49	487.39	531.50
BL2202_B	0.17	0	1000	3	100.0	0.0	49	34.25	37.35
BL2202_B	0.17	10	1000	25	13.3	86.7	49	258.95	282.39
BL2202_B	0.17	20	1000	47	7.1	92.9	49	483.57	527.33
BL2204_A	0.09	0	1000	1	100.0	0.0	49	10.52	11.47
BL2204_A	0.09	10	1000	23	4.5	95.5	49	235.33	256.63
BL2204_A	0.09	20	1000	45	2.3	97.7	49	460.06	501.7
BL2206_A	0.18	0	1000	4	100.0	0.0	49	38.09	41.53

BL2206_A	0.18	10	1000	26	14.6	85.4	49	262.77	286.56
BL2206_A	0.18	20	1000	48	7.9	92.1	49	487.39	531.50
BL2206_B	0.21	0	1000	5	100.0	0.0	49	50.70	55.29
BL2206_B	0.21	10	1000	27	18.5	81.5	49	275.40	300.33
BL2206_B	0.21	20	1000	49	10.2	89.8	49	499.98	545.23
HE2301_A	0.13	0	1000	2	100.0	0.0	49	20.81	22.70
HE2301_A	0.13	10	1000	24	8.5	91.5	49	245.56	267.79
HE2301_A	0.13	20	1000	46	4.5	95.5	49	470.26	512.83
HE2301_B	0.13	0	1000	2	100.0	0.0	49	20.81	22.70
HE2301_B	0.13	10	1000	24	8.5	91.5	49	245.56	267.79
HE2301_B	0.13	20	1000	46	4.5	95.5	49	470.26	512.83
HE2303_A	0.22	0	1000	5	100.0	0.0	49	55.28	60.29
HE2303_A	0.22	10	1000	27	19.8	80.2	49	279.94	305.28
HE2303_A	0.22	20	1000	49	11.1	88.9	49	504.60	550.27
HE2303_B	0.24	0	1000	6	100.0	0.0	49	64.97	70.85
HE2303_B	0.24	10	1000	28	22.5	77.5	49	289.66	315.88
HE2303_B	0.24	20	1000	50	12.7	87.2	49	514.32	560.87
HE2304_A	0.12	0	1000	2	100.0	0.0	49	17.94	19.56
HE2304_A	0.12	10	1000	24	7.4	92.6	49	242.70	264.66
HE2304_A	0.12	20	1000	46	3.9	96.1	49	467.39	509.70
HE2304_B	0.14	0	1000	2	100.0	0.0	49	23.88	26.05
HE2304_B	0.14	10	1000	24	9.7	90.3	49	248.63	271.14
HE2304_B	0.14	20	1000	46	5.1	94.9	49	473.29	516.13
HE2308_A	0.08	0	1000	1	100.0	0.0	49	8.45	9.22
HE2308_A	0.08	10	1000	23	3.6	96.4	49	233.26	254.37
HE2308_A	0.08	20	1000	45	1.9	98.1	49	457.99	499.45
HE2308_B	0.07	0	1000	1	100.0	0.0	49	6.60	7.19
HE2308_B	0.07	10	1000	23	2.9	97.1	49	231.42	252.37
HE2308_B	0.07	20	1000	45	1.5	98.5	49	456.16	497.45